ΠΑΝΕΠΙΣΤΗΜΙΟ ΚΡΗΤΗΣ
ΤΜΗΜΑ ΙΑΤΡΙΚΗΣ
ΕΡΓΑΣΤΗΡΙΟ ΙΑΤΡΙΚΗΣ ΦΥΣΙΚΗΣ
ΔΙΕΥΘΥΝΤΗΣ: ΚΑΘΗΓΗΤΗΣ Ι. ΔΑΜΗΛΑΚΗΣ

ΜΕΤΑΠΤΥΧΙΑΚΟ ΔΙΠΛΩΜΑ ΕΙΔΙΚΕΥΣΗΣ

ΔΙΠΛΩΜΑΤΙΚΗ ΕΡΓΑΣΙΑ

Η Επίδραση του καρδιακού ρυθμού στο CAC Scoring

The effect of heart rate on CAC Scoring

Ιωάννης Ανδρουλάκης

ΕΠΙΒΛΕΠΩΝ
ΚΩΝΣΤΑΝΤΙΝΟΣ ΠΕΡΙΣΥΝΑΚΗΣ
ΑΝΑΠΛΗΡΩΤΗΣ ΚΑΘΗΓΗΤΗΣ ΙΑΤΡΙΚΗΣ ΦΥΣΙΚΗΣ

ΗΡΑΚΛΕΙΟ, 2017

ΔΙΑΠΑΝΕΠΙΣΤΗΜΙΑΚΟ ΔΙΑΤΜΗΜΑΤΙΚΟ
ΠΡΟΓΡΑΜΜΑ ΜΕΤΑΠΤΥΧΙΑΚΩΝ ΣΠΟΥΔΩΝ ΣΤΗΝ
ΙΑΤΡΙΚΗ ΦΥΣΙΚΗ – ΑΚΤΙΝΟΦΥΣΙΚΗ

The effects of heart rate on coronary artery calcium scoring

Ioannis Androulakis

Abstract

Objective: The purpose of this study was to investigate the effect of heart rate on the coronary artery calcium (CAC) score estimate provided by a modern 64-slice multi-slice CT system.

Methods and Materials: Cylindrical calcified lesion phantoms of varying size and calcium concentration were constructed to mimic atheromatic plaques occurring in atheromatous patients. These artificial athermomatic lesions were introduced into a dynamic anthropomorphic cardiac phantom which has the ability to produce three dimensional recurrent movement with heart rate defined by the user. The motion of coronary arteries, and consequently the atheromatic plaque(s) developed in the arteries, was thus simulated. The cardiac phantom loaded with the atheromatic lesions was subjected to the standard 120 kVp cardiac CT examination protocol and image series were acquired for different heart rates in the range 40-100 bpm. The Agatston score (AS), the calcium mass score (CMS), the calcium volume (CVS) and calcium density score (CDS) were estimated for each image dataset using a dedicated processing software package.

Results: The AS and the CMS were found to considerably decline with increasing heart rate. The coefficient of the linear function of CAC score against heart rate was found to be -0.2±0.1% and -0.4± 0.0% per 1 bpm for AS and CMS, respectively. CVS and CDS were found to irregularly be affected by heart rate. The size of lesions was found to be associated with the level of decline in calcium scores with increasing heart rate. The decline of CMS with increasing heart rate was found to be steeper for smaller size lesions and for lower calcium concentrations.

Conclusion: The AS, CMS, CVS and CDS are dependent on heart rate. Scores tend to decline for higher heart rates. The size as well as the calcium concentration of atheromatic lesion affect the decline of calcium scores with increasing heart rate.

Contents

Acknowledgments

This master thesis is my last task for the completion of the master program in Medical Physics/Radiation Physics.

I would hereby want to thank, first of all, Mr. Perisinakis for assigning me this project, for his excellent guidance and for the hours we spent talking about and working on this project.

I would also want to thank Mr. Papadakis for his help in completing the experimental part of the project and Mr. Damilakis for the care he took, as head of the Medical Physics department, for me and the rest of the master students at the department.

Furthermore I thank my friend A. Stoyanov for his help in the material construction; the secretary of the master program, Mrs. Dalles; my colleagues at the master program; and of course my parents for their unlimited support.

Ioannis Androulakis

Part I

General Part

Chapter 1

X-ray Physics

1.1 X-ray generation

1.1.1 Bremsstrahlung

Bremsstrahlung is an electromagnetic radiation, produced by the interaction of fast electrons with matter. The higher the electron's speed (energy), the higher the fraction of the electron's energy that converts into Bremsstrahlung. The production of Bremsstrahlung becomes larger as the absorbing material's atomic number increases.

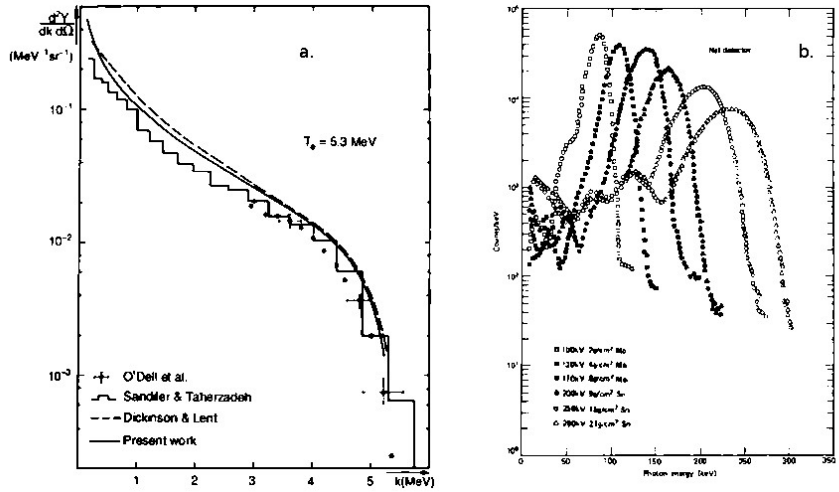

Figure 1.1: *a. The bremsstrahlung energy spectrum emitted by the interaction 5.3 MeV electron beam with a Au-W target. The photons pass through a* $7.72 g/cm^2$ *aluminum filter. b. Filtration of a bremsstrahlung beam by different absorbers.* [1]

Electrons of a given energy that collide with a material produce a continuous electromagnetic spectrum with energies that span from 0 to the electron's energy, in a shape given in Figure 1.1.a. As can be seen in the figure, the mean energy of the spectrum is low, compared to the electron energy. The energy spectrum can be altered towards higher mean photon energies through the means of filtration and the passage through absorbing materials. These materials absorb the lower photon energies, producing a peaky distribution of the energy spectrum as given in Figure 1.1.b.

When the target material is thin, so that no electron interacts more than once with the target, then a theory suggests that the energy radiated in form of Bremsstrahlung is proportional to EZ, where E represents the electron's energy and Z is the atomic number of the target. This theory is accurate for electron energies up to about 100keV, but only approximately correct for higher energies.[2]

For thick targets, the equation giving the intensity of radiated photons is

$$I(E) = CZ(E_{max} - E) \tag{1.1}$$

where $I(E)$ is the intensity at energy E, E_{max} is the maximum photon energy, which is equal to the electron beam's energy, Z is the atomic number of the target and C represents a constant.[2]

Bremsstrahlung is commonly produced through X-ray tubes (see 1.1.3). In an X-ray tube, characteristic X-rays (see 1.1.2) are also produced if electron energy is high enough. Therefore the electromagnetic spectrum from X-ray tubes is usually a blend of bremsstrahlung together with Characteristic X-rays.

1.1.2 Characteristic X-rays

When an orbital electron of an atom is removed from its natural position due to an excitation process, the orbital electrons tend to rearrange themselves in order to return to the atom's lowest energy state (or ground state). The energy from this rearrangement is released in the form of photons called *characteristic X-rays*. The energy given to these photons is equal to the binding energy difference between the excited and ground state of the atom. For example, if an electron is removed from the K-shell of the atom and the hole is filled with an L-shell electron, then a photon called K_α is released with an energy equal to $E_K - E_L$. If instead the hole is filled by an M-shell, the the photon is called K_β.

According to which of the L-subshells gives the electron to the K-shell, we have K_{α_1} and K_{α_2} photons from shells L_{III} and L_{II}. Due to quantum physics laws, not all transitions between subshells are permitted. Therefore, for example, although we have three subshells in L, there are only two transitions to the K-shell, namely K_{α_1} and K_{α_2}.

The energy of characteristic X-rays increases according to the atomic number of the element that produces them. The most significant characteristic X-rays are K_α, due to their superior energy. The L series have much lower energies; namely, they do not reach 1 keV until Z=28.

Shell	Oxygen Z = 8	Calcium Z = 20	Copper Z = 29	Molybdenum Z = 42	Tin Z = 50	Tungsten Z = 74	Lead Z = 82
K	.533	4.037	8.981	20.000	29.200	69.525	88.004
L_I	.024	1.438	1.096	2.867	4.465	12.098	15.861
L_{II}	.009	.350	.953	2.625	4.156	11.541	15.200
L_{III}	.009	.346	.933	2.521	3.929	10.204	13.035
M_I	—	.044	.122	.505	.884	2.820	3.851
M_{II}	not	.025	.074	.410	.756	2.575	3.554
M_{III}	filled	.025	.074	.392	.714	2.281	3.066
M_{IV}	—	—	.007	.230	.493	1.871	2.586
M_V	—	—	.007	.228	.485	1.809	2.484

Table 1.1: critical X-ray absorption energies (keV)[2]

K Lines Tungsten				L Lines Tungsten			
Transition	Symbol	Energy (keV)	Relative Number	Transition	Symbol	Energy (keV)	Relative Number
$K\text{-}N_{II}N_{III}$	$K\beta_2$	69.081	7	$L_I\text{-}N_{III}$	$L\gamma_5$	11.674	10
$K\text{-}M_{III}$	$K\beta_1$	67.244	21	$L_{II}\text{-}N_{IV}$	$L\gamma_1$	11.285	24
$K\text{-}M_{II}$	$K\beta_3$	66.950	11	$L_{III}\text{-}N_V$	$L\beta_2$	9.962	18
$K\text{-}L_{III}$	$K\alpha_1$	59.321	100	$L_I\text{-}M_{III}$	$L\beta_3$	9.817	37
$K\text{-}L_{II}$	$K\alpha_2$	57.984	58	$L_{II}\text{-}M_{IV}$	$L\beta_1$	9.670	127
K lines Molybdenum				$L_I\text{-}M_{II}$	$L\beta_4$	9.523	29
$K\text{-}M_{II}M_{III}$	$K\beta_{31}$	19.602	24	$L_{III}\text{-}M_V$	$L\alpha_1$	8.395	100
$K\text{-}L_{III}$	$K\alpha_1$	17.479	100	$L_{III}\text{-}M_{IV}$	$L\alpha_2$	8.333	11
$K\text{-}L_{II}$	$K\alpha_2$	17.375	52				

Table 1.2: Emission Lines in keV for Tungsten (Z=74) and Molybdenum (Z=42).[2]

Characteristic radiation is a competitive process to Auger electron emission, therefore not all de-excitations produce characteristic X-rays. The fluorescent yield is therefore defined as the fraction of the de-excitations that produce photons.

Since characteristic radiation occurs due to the existence of excited states in an atom, the processes that lead to these excited states are of importance in its study. There are a lot of different processes that can lead to excited atomic states, including excitation due to nuclear decay with electron capture, due to internal conversion and due to the interaction of an external source of radiation (X-rays, electrons, heavy charged particles, etc.) with a target material.[1]

1.1.3 X-ray Tubes

In medical applications, the production of X-rays is usually performed through an *X-ray Tube* (see Figure 1.2). In an X-ray tube, a high voltage

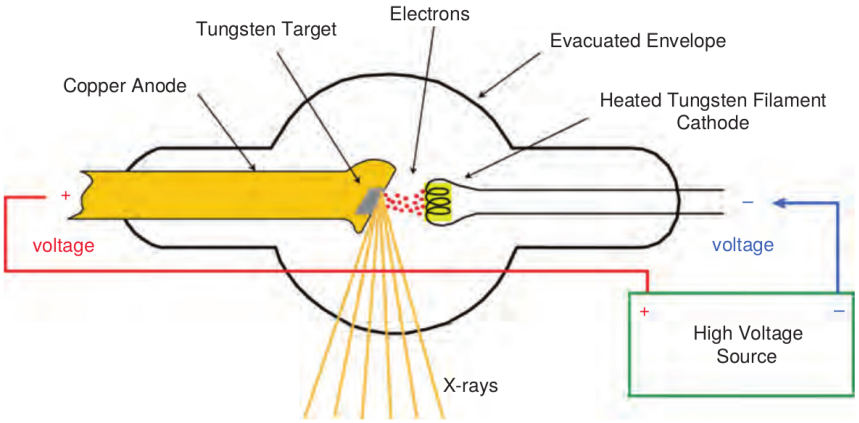

Figure 1.2: *The general concept of an X-ray tube.* [3]

source is connected to a tungsten filament wire, called *the cathode* and a metal target electrode called the *anode*, which is facing the cathode. Both the anode and cathode are inside an airtight vacuum tube.

The cathode is negatively charged, while the anode holds a positive voltage with respect to the cathode. At a high enough potential difference, electrons start leaving the heated cathode and accelerate towards the positive anode, in a process called *thermionic emission*. When electrons fall onto the anode's target, X-rays are produced; namely Bremsstrahlung and Characteristic X-rays.

Thermionic emission happens when the filament is heated to approximately T=2400K[4]. On these temperatures the energy kT given to the electrons of the filament is enough to overcome their binding energy. Therefore they become free electrons and consequently start moving towards the positive charge of the anode.

Cathode

The cathode is usually surrounded by and electrically connected to a structure called the *focusing cup*, which is charged, providing a voltage to the filament in order to heat it. This process produces the heat needed for thermionic emission.

The focusing cup is also responsible for the shaping of the electron beam. The focusing cup can either have the same voltage as the filament, or be *biased*. In the latter case a negative voltage with respect to the filament is applied to the focusing cup, in order to reduce the spatial distribution of the electron beam.

Anode

The anode electrode is usually made out of copper, with a small (usually) tungsten target directly opposite to the cathode filament. Most of the electrons that fall onto the tungsten target produce heat, with only a small 1% fraction converting into X-rays. With tungsten having a high melting point and a high atomic number, it becomes an effective target material and is therefore widely used. Other target materials are Molybdenum and Rhodium, but are less common.

There are two basic anode configurations, namely *stationary* and *rotating*. The first is more simple, consisting of a tungsten insert mounted into a copper block. Heat is removed by conduction into the copper block. The more complex rotating anode is developed in order to be able to absorb more heat. It is therefore used in applications which require higher x-ray output capabilities. In the rotating anode, the tungsten target is disk-shaped and larger. The target disk is continuously rotating and therefore heat is transferred through the whole anode disk. The disk is mounted onto a rotor through a molybdenum stem which is surrounded by electromagnets in a system called the *induction motor*.

When electrons hit the anode target the produced X-ray beam is usually steered in a right angle towards an exit. The anode therefore shapes an angle towards the cathode of about 7 to 20 degrees. The larger the target angle, the wider the X-ray beam becomes, while the beam becomes thinner with a small angle. The cathode also plays a role in beam shape, with a smaller filament length resulting in a better focused X-ray beam.[5]

Heat

Since almost 99% of the energy used in an X-ray tube is converted into heat, an X-ray tube has to be able to to absorb this heat. This ability is related to the thermal capacity of the tube. If the tube gets overheated it has to stop operating in order to cool down. Therefore its ability to store heat, measured in *Heat Units, HU* and its cooling rate (thermal abduction), measured in *HU/min* are important parameters of a tube, especially if it needs to operate for long periods, as is the case in X-ray Fluoroscopy and CT.

Tube Insert and Housing

The discussed parts of the X-ray tube are all enclosed into a glass or metal vacuum. This minimizes the interactions of electrons with air molecules. The enclosure is called a *tube insert*. The tube insert is enclosed into a housing with oil in order to insulate and protect it from overheating. The oil of the housing absorbs the produced heat and around the oil a lead shield it attenuates the radiation emitted to non-useful directions.

Filtration and Collimation

The energy spectrum of the photons (see 1.1.1) produced by the X-ray tube varies from 0 to an energy equal to the electron energy of the tube,

$$eU_a = hv_{max} = E_{max} \tag{1.2}$$

This means that a lot of low energy photons are produced, which are usually not useful. Therefore, the X-ray beam passes through a thin (1-2mm) aluminum(Z=14) or glass(Z=13) *filter*. These materials have a relatively small atomic number and therefore absorb the low energy spectrum, leading to a higher average beam energy.

The size adjustment and shaping of the X-ray beam is performed by *collimators*. Collimators consist of lead(Z=82) and absorb all the unnecessary parts of the beam.

1.2 Interaction of photons with matter

1.2.1 Attenuation

When a material is placed in the way of a photon beam, each photon develops a chance of interacting with the material. When a photon interacts with the material, it is consequently removed from the beam, regardless the type of interaction that occurs. In other words a photon can not be partially stopped by a material. It will either come close enough to the atom of the material and be removed from the path of the beam through interaction, or it won't interact at all and continue it's path.

Describing the above in a mathematical way, when a beam consisting out of N photons passes through a Δx thick material, the drop in photons, ΔN is equal to

$$\Delta N = -\mu N \Delta x \tag{1.3}$$

where μ is a constant, called *linear attenuation coefficient*, and represents the proportion of photons per unit thickness of given material that interact with it. This equation is strictly correct only when $\mu \Delta x \ll 1$. Therefore it is more correct to rewrite 1.3 in differential form, as

$$dN = -\mu N dx \tag{1.4}$$

Equation 1.4 can be solved into

$$N = N_o e^{-\mu x} \tag{1.5}$$

where N_0 is the number of photons before the interaction and N is the number of photons after the beam passes an x thickness of material. The latter equation represents the exponential form of photon attenuation in matter, otherwise named Beer's law. It may also be written in beam intensity form, as

$$I(x) = I_o e^{-\mu x} \tag{1.6}$$

	muscle $\bar{Z} = 7.64$ $\rho = 1040\ kg/m^3$		bone $\bar{Z} = 12.31$ $\rho = 1650\ kg/m^3$	
energy (keV) hv	mass attenuation coefficients $[cm^2/g]$ (μ/ρ)	linear attenuation coefficients $[cm^{-1}]$ μ	mass attenuation coefficients $[cm^2/g]$ (μ/ρ)	linear attenuation coefficients $[cm^{-1}]$ μ
10	5.154	5.360	19.79	32.65
50	0.224	0.233	0.347	0.573
80	0.182	0.189	0.208	0.344
100	0.169	0.176	0.180	0.297
150	0.149	0.155	0.149	0.246
200	0.136	0.141	0.133	0.220
500	0.092	0.096	0.093	0.153

Table 1.3: attenuation coefficients for different materials [2]

where I_o the intensity of the beam before the interaction and $I(x)$ the beam intensity after a distance x into material with a μ linear attenuation coefficient.

The linear attenuation coefficient is dependent on the density and atomic number of the material, as well as the energy of the photon beam. Its units are reversed length units, usually cm^{-1} or m^{-1}. The attenuation of a given material can be found in tables, usually in the form of *mass attenuation coefficient* μ/ρ.[6] Table 1.2.1 shows the attenuation coefficients for two different human tissue for different energies.

Equation 1.6 is valid for photon beams of relatively small diameters. Such beams are called narrow beams or good geometry beams. When the beam diameter becomes broader, an additional parameter, called the *buildup factor* (B), is multiplied with the exponential term.

$$I(x) = I_o B e^{-\mu x} \tag{1.7}$$

This factor is dependent on the beam geometry, the geometry of the absorber, the photon energy and the atomic number of the absorbing material.[2]

Photons interact with matter mainly through three mechanisms of interaction, all of which are energy dependent. The *photoelectric absorption* is the main interaction in lower photon energies, the *Compton scattering* is the main interaction in medium photon energies, while *pair production* begins at energies over 1 MeV. Besides these three, another type of interaction called *coherent scattering* takes place, mainly in lower energies (see figure 1.3). The basic properties of the photon-matter interaction processes will be discussed in the following sections.

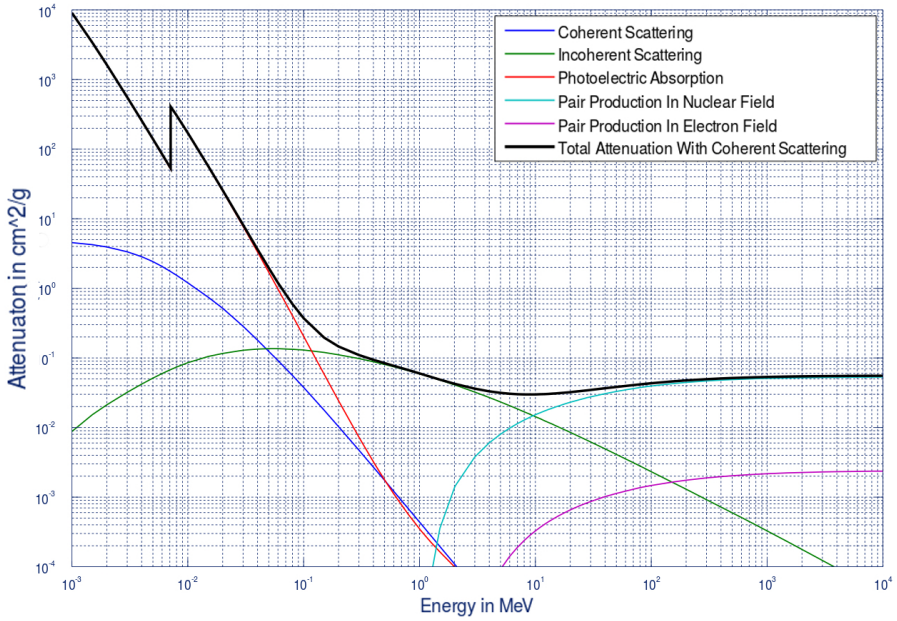

Figure 1.3: *Mass attenuation coefficient to photon energy diagram for Iron (Z=26)*

1.2.2 Photoelectric Absorption

In the photoelectric absorption process, a photon interacts with an atom, releasing all it's energy into the atom, while releasing a bound electron from its shell. The interaction can only take place, when the photon energy hv is at least equal to the binding energy E_B of the electron. Since the photon releases all its energy into the atom, it consequently disappears. The electron that is released from the atom is called a *photoelectron* and bears a kinetic energy of

$$E_{e^-} = hv - E_b \tag{1.8}$$

For photons with sufficient energy, the most probable electron to leave the atom is one originating from the inner K-shell.

The photoelectric absorption leaves the atom with one less electron, leading to an ionized atom. The vacancy is filled with an electron from the outer layers of the atom and it finally de-excitates with the absorption of a free electron. This process may lead to the production of additional characteristic X-rays or Auger electrons.

The probability of the photoelectric absorption process is energy dependent, with a maximum probability when the photon energy is just over the binding energy of the electron. This leads to attenuation coefficient peaks just

over the binding energies of the absorber's shells (see figure 1.3). The cross section varies with photon energy approximately at $1/(h\nu)^3$.

Further, the process has also a strong probability connection with the atomic number of the absorbing material. For low Z materials, the coefficient varies as much as $Z^{3.8}$ per electron and $Z^{4.8}$ per atom, while for high Z materials it varies at Z^3 per electron.

An empirical equation for the photoelectic atomic absorption coefficient, is:

$$\tau_\alpha \propto \frac{Z^{4.5}}{h\nu^3} \tag{1.9}$$

and for the mass attenuation coefficient:

$$\left(\frac{\tau}{\rho}\right) \propto \left(\frac{Z}{h\nu}\right)^3 \tag{1.10}$$

1.2.3 Compton Scattering

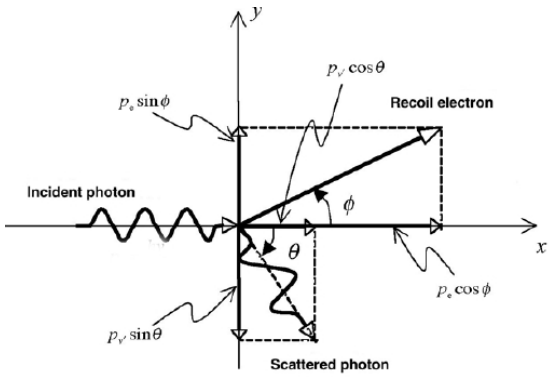

Figure 1.4: *Graphical representation of the Compton scattering interaction*

In Compton scattering (see figure 1.4), a photon interacts with a loosely bound electron in the absorbing material. The incident photon, $h\nu$, transfers a portion of its energy to the electron, E, called *recoil electron*, and changes its direction at an angle θ carrying the remaining energy, $h\nu'$. Compton scattering is also referred to as incoherent scattering. The process is almost independent from the atom itself and therefore usually regards the electron as free.

The energy of the scattered photon, regarding the electron as free, is

$$h\nu' = \frac{h\nu}{1 + \frac{h\nu}{m_o c^2}(1 - cos\theta)} \tag{1.11}$$

where $m_o c^2$ is equal to $511keV$ (the rest mass of the electron). The $h\nu - h\nu'$ energy difference is given as kinetic energy to the recoil electron. As can be seen,

the larger the scattering angle θ, the more energy is transferred to the electron. The scattered photon distribution ranges between a minimum of $hv\frac{1}{1+hv/m_oc^2}$ and a maximum of hv, for $\theta = \pi$ and $\theta = 0$ respectively.

The probability of a photon interacting in a Compton interaction (σ) is described by the Klein-Nishina equation, in which the differential cross section ($d\sigma/d\Omega$) is

$$\frac{d\sigma}{d\Omega} = \frac{{r_0}^2}{2}(1 + cos^2\theta)F_{KN} \tag{1.12}$$

where r_0 is the classical electron radius and F_{KN} is the Klein-Nishina factor, which equals to

$$F_{KN} = \left[\frac{1}{1+\alpha(1-cos\theta)}\right]^2 \left[1 + \frac{\alpha^2(1-cos\theta)^2}{(1+a(1-cos\theta))\,(1+cos^2\theta)}\right] \tag{1.13}$$

where $\alpha = hv/m_oc^2$.

Generally, the fraction of the energy transferred to the recoil electron increases with an increase in incident photon energy. For low energy photons $\sigma_{tr} \ll \sigma$, while for high energy photons $\sigma_{tr} \simeq \sigma$.

As can be seen in figure 1.3, where Compton scattering is referred to as incoherent scattering, its contribution to the attenuation becomes most important for the medium energy spectrum.

1.2.4 Pair Production

When a photon has energy at least equal to twice the rest mass of the electron (1.022MeV), it may be absorbed through a process called pair production. This mechanism involves an interaction with the field of the absorber atom's nucleus. The photon is absorbed and a electron-positron pair is released. The photon therefore has to be able to give at least the positron's and electron's rest masses in energy, leading to an energy threshold of $2 \times 511keV$ for the incident photon. The remaining energy is shared between the positron and the electron, as

$$hv - 1.022MeV = E_+ + E_- \tag{1.14}$$

where E_+ and E_- are the positron and electron kinetic energies respectively. The energy division between the two particles can vary. So does the direction of the two particles.

The positron, as an antiparticle, has a limited half-life and when it is slowed down ionizing atoms, it collides with a free electron producing two annihilation photons, each of $511keV$ energy, towards opposite directions.

A variation of pair production is the triplet production. The latter process is performed into the field of the electron rather than that of the nucleus. The energy is now split among the created electron, the positron and the original electron, forming a triplet.

The pair production cross section κ is increased with the increase in photon energy. This means that a higher energy photon is more likely to interact

in a pair producing process with the nucleus, than a lower energy photon. This is not the case in the other two processes described.

The higher the atomic number of the absorber, the higher the pair production probability. Pair production coefficient varies approximately as Z^2 per atom and Z per unit mass.

1.2.5 Coherent Scattering

Coherent scattering is a photon interaction in which no energy is transformed into kinetic energy, and all is scattered. When a photon passes near an electron, the electron absorbs its energy, it momentarily accelerates and then radiates the absorbed energy towards another direction. This process is called Thomson or Classical Coherent Scattering. The distribution of the Thomson scattering coefficient per electron per unit solid angle is

$$\frac{d\sigma_0}{d\Omega} = \frac{{r_0}^2}{2}(1 + cos^2\theta) \tag{1.15}$$

and looks similar to the Compton scattering equation, if we remove the Klein-Nishina factor. The Thomson scattering is described with classical physics.

When in coherent scattering we take into account the interaction with the field of the atom, we have an interaction called Rayleich Scattering. The process is important when low energy photons interact with high atomic number materials (see blue line in figure 1.3). The distribution of the Rayleich scattering coefficient is

$$\frac{d\sigma_{coh}}{d\theta} = \frac{{r_0}^2}{2}(1 + cos^2\theta)[F(x, Z)]^2 2\pi sin\theta \tag{1.16}$$

where $x = (sin\theta/2)/\lambda$ and $F(x, Z)$ is a term called atomic form factor.

1.2.6 Total Attenuation Coefficient

The total attenuation coefficient can be broken down into all the different attenuation coefficients, corresponding to the different interaction processes available. The sum of these separate attenuation coefficients is then equal to

$$\begin{array}{ccccccccc} \mu & = & \tau & + & \sigma_{coh} & + & \sigma_{inc} & + & \tau \\ & & \text{photoelectric} & & \text{coherent} & & \text{incoherent} & & \text{pair} \\ & & \text{absorption} & & \text{scattering} & & \text{scattering} & & \text{production} \end{array}$$

which includes all the possible interactions making up the total interaction coefficient. In figure 1.3 we can see the relation between the total attenuation coefficient and the coefficients of each interaction for different energies.

1.3 Photon Detection

X-rays can be detected through the products that are produced when they interact with matter. X-ray detectors are therefore devices that are able

to cause an interaction and collect the interaction products in the form of an electric pulse.

Modern detectors are separated into three basic categories, based on their characteristics, namely *Gas Detectors*, *Scintillation Detectors* and *Solid State Detectors*.

In *Gas Detectors*, the material that interacts with the radiation is an appropriate gas type, on which we are able to apply a voltage. The radiation produces ion pairs into the gas, which we are able to collect and measure through the applying voltage. In this way the produced ions are converted into an electric pulse and thus give us information about the photons that have passed through and interacted with the detector.

Scintillation Detectors consist out of a material who has the ability to interact with a photon producing a visible or near-visible light spark. The photons produced by the spark are collected through devices, called *photomultipliers*, and converted into electric pulses.

The last category of photon detectors, *Solid State Detectors*, uses semiconductor materials to detect photons. The interaction process is similar to gas detectors, but instead of ion pairs they use electron-hole pairs. The electrons and holes are again collected through an applied voltage and produce electric pulses representing photon-detector interactions.

Chapter 2

Tomography

Since it's early days, Computed Tomography, *CT*, has greatly contributed to medicine as a diagnostic tool. Starting as a brain imaging modality it has managed to evolve throughout the years into a tool with many clinical applications, including oncology, vascular radiology, cardiology, traumatology and interventional radiology.

2.1 Early History

X-rays have since it's discovery, been very closely related to human body imaging. Wilhelm Roentgen, the first researcher to systematically study X-rays, produced the first picture in 1895, depicting the hand of his wife on a photographic plate. He noticed that X-rays had the ability to pass through soft tissue, but not through the bones nor metal. One year later, in 1896, the first clinical uses had already begun.

2.1.1 Conventional Tomography

While radiography was becoming a routine examination in the early 20th century, researchers had to deal with the problematic imaging of complex structures within the human body. Radiographing such structures resulted in a superimposition of all the organs between the cathode and the film, making it difficult to produce a clinically useful image. Some of the solutions proposed were depiction of the region of interest from different projections, the addition of contrast media to the organs of interest and changes in body positions and dynamics during fluoroscopy. [7]

A resolution of this problem was also found in the idea of body section radiography [7], an idea that would slowly evolve into a very powerful diagnostic tool. The idea of body section radiography is the depiction of a layer of the human body, while all structures outside this layer are being excluded.

The first attempts of body sectioning were performed with mechanical

means. These attempts that would result in a series of imaging devices, are today all together described as Conventional Tomography. The early history of conventional tomography, though, is more complicated than it seems today. Characteristically, the early pioneers of conventional tomography all gave a different name (planigraphy, stratigraphy, tomography, laminagraphy, X-ray focusing machine) to their technique of body sectioning, while in most cases not being aware of developments of the same technique in other parts of the world.

The basic concept of Conventional Tomography describes an imaging system into which two out of the three imaging elements (source, body, capturing device) move in a certain way, in order that a certain slice of the body remains imaged on the film with the same geometry, while the projection of other parts of the body changes geometry. This concept allows the blurring of the other parts of the body on the film, while the target slice remains sharp. Usually this is achieved with the use of a static body and an aligned movement of the film and the x-ray source.

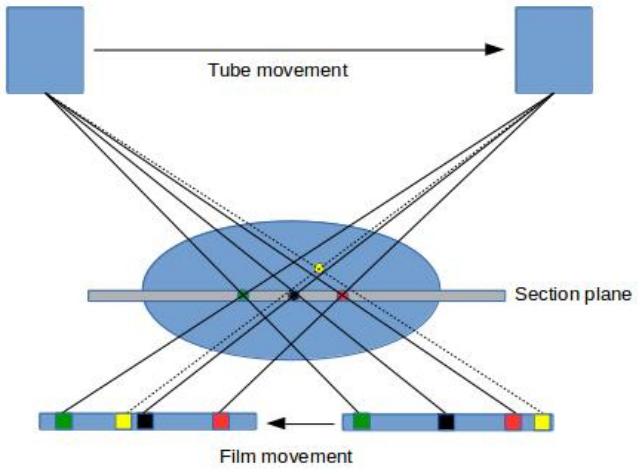

Figure 2.1: *2D representation of the basic principles of Conventional Tomography*

The first theoretical description of a tomographic system was performed as early as in 1921. The French dermatosyphilologist, Andre-Edmund-Marie Bocage filed a patent that year that contained the basic design principles of a tomographic device. The device was designed to perform circle and spiral tube-film movements, while the tube-film ratio remained constant. The scatter rays of the tube were to be eliminated and the beam diameter should be small. The design was never really constructed and Bocage would practically see a tomographic machine much later at a presentation of manufacturer Jean Massiot in 1935. This meeting, although would lead to the Biotome, a device built by Massiot's father in honor of Bocage. It would imply a lot of Bocage's ideas on tomography and be designed for chest tomography.[7]

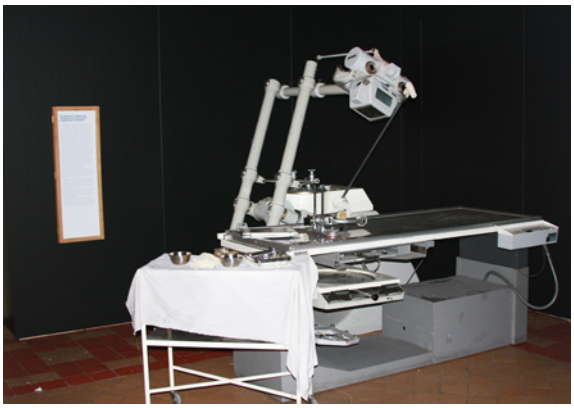

Figure 2.2: *The Polytome, acquired from: www.radiology-museum.be*

Although the earliest theoretical description was made by Bocage, the first working tomographic apparatus was built by Alessandro Valebona, the director of the Radiological Institute of the University of Genoa. He called his apparatus a stratigraph and presented an experimental device able to image a dried skull in 1930. In 1933 he was also able to present a device for clinical use. After that, he continued his research and teaching throughout the history of conventional tomography.[7]

Another great experimenter was Georg Ziedses des Plantes, a neurologist and later a radiology professor at the University of Amsterdam. He also independently developed a conventional tomographic device presenting clinical results one year later than Valebona, in 1931. His apparatus, the so called planigraph, had spiral and circular tube-film movements, and worked primarily with phantoms and skulls. The Polytome design was later based onto Ziedses des Plantes' work. He, like Vallebona, also continued contributing to tomography throughout his life.[8] [7]

Other independent inventors of conventional tomography were Gustav Grossmann from Germany, who patented the Tomograph in 1934 and Jean Kieffer from the USA, who patented the "X-ray Focusing Machine" in 1929 (granted in 1934). Together with Sherwood Moore, Jean Kieffer developed the first American built tomographic device, called the Kele-Kieffer Laminagraph. [7]

In the early days of tomography work was put only into coronal and sagital slicing. The first axial noncomputed tomographic images were produced by British radiographer William Watson in 1937, from a device with a stationary tube called the sectograph. The device later became commercial.[9]

The first real breakthrough of conventional tomography was in the years after WWII. In the 50's a lot of sophisticated pluridirectional devices appeared, in contrast to the simple linearly moving early devices[7]. The first of them, the Polytome, marked the start of this era of very accurate tomographic images. It

produced images with high contrast, excellent spatial resolution and very thin slices (1mm)[7]. After the production of the Polytome, many manufacturers produced their own tomographs, leading to a thriving era for conventional tomography until the late 80's, when attention was steered more towards the new technologies of computed tomography and magnetic resonance imaging.

2.1.2 Computed Tomography

In 1917, Austrian mathematician Johann Karl August Radon, found that an infinite number of two-dimensional projections of an unknown object could be reconstructed into a three-dimensional image of that same object. His method would become known as the Radon transform and would become the theoretical basis of Computed Tomography (CT). [10]

It required a lot of years and a lot of technological advances since the description of the Radon transform, for the next step in CT to take place. This was done by South African physicist Allan MacLeod Cormack. Cormack developed the theoretical basis of CT scanning in two publications in 1963 and 1964, without knowing about Radon's theory. [10]

In 1968, researcher Godfrey Hounsfield and a small group of colleagues started a laboratory in Hayes, England. Hounsfield and his group were working under the EMI Corporation and had never worked in the X-ray business before. Despite that, they started working on a prototype apparatus that would be able to obtain two-dimensional data from various phantoms and reconstruct it with computer techniques. Although the first image required nine days of scanning time and two-and-a-half hours of computing time, the reconstructed image showed promise and motivated for further effort. Finally a clinical prototype unit was produced that required a scanning time of four-and-a-half minutes for each slide but could only be used for head imaging. This prototype was able to produce images of reasonable resolution, so it was placed into the Atkinson Morley Hospital in 1971, leading to the first clinical use.[10] [11] [12]

The Mark 1, as EMI's unit was called excited the medical community although it was a quite primitive apparatus compared to what CT is today. It required long scanning times per slice and was only suitable for head scans. The device produced 80x80 pixel images (3mm pixels) and each pair of slices required 4.5 minutes of scanning time and 1.5 minutes of reconstruction time. Because of the long acquisition times, the head had to be in a fixed position[5]. Furthermore, the head had to be placed in a rubber sack full of water in order to deal with homogeneity issues[10].

CT received great attention due to it's impact on neuroradiology. It was the first time a device could take images of the brain's ventricles without the use of contrast material. In a few months time, everyone, from physicians to reporters and presidents, knew about this new technology. Consequently, a Nobel price was awarded to Cormack and Hounsfield in 1979 and a lot of research was put into the improvement of CT.[10]

Because of the long scanning times in combination with respiratory motion, no one had really believed in the early days of CT, that the device would

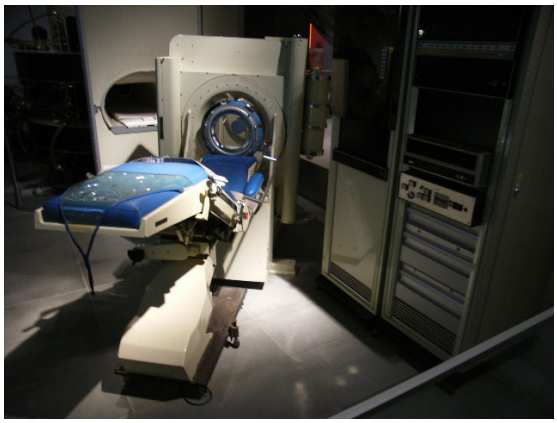

Figure 2.3: *EMI's first commercial CT head scanner.*

develop into a full body scanner like it is today. Advances in computing power detector technology and tube design, in combination with multiple detector arrays and other acquisition techniques, have today led to very fast acquisition times and real-time reconstruction.[5]

2.2 Principles of Computed Tomography

2.2.1 General Properties

The CT process involves the rotation of an X-ray tube and a detector row around the patient. The detector row collects the transmission profiles through the patient as the tube rotates, providing data from a lot of different orientations around the patient. A single transmission measurement from a single detector element is called a *ray*. All rays that are collected from the same orientation generate the so called *view* or *projection*.

From a mathematical standpoint, the CT concept can be described as the visualization of an object through its projections. The CT scanner collects a large number of transmission measurements through the patient at different positions. The collected data from the different projections of the same axial slice is used for the reconstruction of the CT image, which consists of a matrix of picture elements (pixels). A slight movement of the patient table in the cranial-caudal direction, the scanner's z-axis, allows the CT system to collect data for consecutive slices.

2.2.2 Collected Data

According to Beer's law (1.6), the intensity of an X-ray beam that passes through a material is equivalent to

$$I(x) = I_o e^{-\mu x} \tag{2.1}$$

where I_o is the unattenuated intensity of the beam, x is the material's thickness and μ is the linear attenuation coefficient of that material. The linear attenuation coefficient depends on the atomic composition and density of the material, but also on the energy of the beam.

Although the detectors in CT measure X-ray intensities, the collected data is related to the linear attenuation coefficient of the tissue through which each ray passes. As the human body is generally inhomogenous, the beam passes through different tissues with different attenuation values. If the beam's path stretches from 0 to d, then the intensity of the X-ray beam across it's path, according to Beer's law (2.1), becomes

$$I(d) = I_o e^{-\int_0^d \mu(x)dx} \tag{2.2}$$

and since the CT data is stored as a matrix of picture elements, it is safe to discretisize the attenuation coefficient into a matrix of discrete attenuation coefficients. Therefore (2.2) may be written as

$$I(d) = I_o e^{-\sum_{i=0}^{n} \mu_i \Delta x} \tag{2.3}$$

That makes it clear that the basic data needed in order to acquire the attenuation matrix are the unattenuated (I_o) and attenuated ($I(d)$) beam intensities. The methodologies used in order to switch from beam intensities to attenuation coefficients are various and are analyzed below in 2.5.

Beer's law describes only the intensity of the primary beam of a given energy value, ignoring any secondary intensities. This means that Beer's law should normally be integrated for all energies in the X-ray spectrum. Practically, however, it is applied only once on the value representing the average beam energy. This shortcut however leads to the beam hardening artifact.

2.2.3 Hounsfield Units

The values used in CT are not exactly the linear attenuation coefficients of the tissue, but rather a relative unit called after it's inventor, Hounsfield. The *Hounsfield Units* (HU) or *CT Numbers* are scaled relative to the linear attenuation coefficient of distilled water at standard pressure and temperature (μ_{water}) [12]. The relation between a tissue's linear attenuation coefficient and it's HU is

$$HU_{material} = \frac{\mu_{material} - \mu_{water}}{\mu_{water}} \times 1000 \tag{2.4}$$

where we can see the typical values of $HU_{water} = 0$, $HU_{air} = -1000$ ($\mu_{air} = 0$). Typical values of human tissue are around 1000 for compact bone, 50 for most

soft tissues, -90 for fat and -750 for lung tissue. The HU normalization results in values from about -1000 to +3000 in human body imaging. The minimum bit depth that should be assigned to a pixel is therefore 12. This allows each pixel to take a value from -1024 to +3071.[11]

2.2.4 Visualization of the collected data

The visualization of the pixel values is performed in a scale of 8 bits, delivering 256 shades of gray. The reduction of the 12 bits of image data to the 8 bit scale is performed through the processes of *windowing and leveling*[5]. Windowing stands for determining the range of the imaged HU data, known as the display window. This process controls the contrast of the image. The leveling process changes the HU value of the center of the display window. Different windowing and centering settings are needed in order to visualize different tissue types.

2.2.5 Beam Geometry

Three different geometries have been applied in CT. The first geometry in which all projections are parallel to each other is called *parallel beam geometry*. The second used geometry is called *fan beam geometry*. In this one the rays in one projection diverge in a fan-like geometry. *Cone beam geometry* is the last geometry that appeared in CT. In cone beam geometry, the beam diverges in two dimensions, shaping a cone-like shape.

2.2.6 Gantry and Patient Table

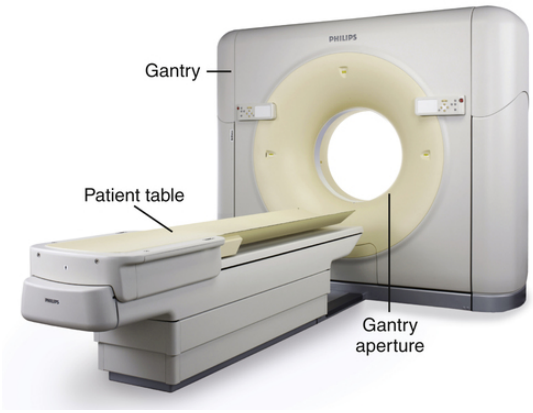

Figure 2.4: *The gantry, gantry aperture, and patient table. (Courtesy Philips Medical Systems.)*

The *gantry* represents the part of the CT that contains all the system components required for the data acquisition, namely the X-ray tube, its collimation and beam shaping system and the detector system. Since the transmission profiles have to be acquired from different angles, the gantry includes a rotating part and has a ring shape. Modern CT systems develop very high rotation velocities, therefore the gantry has a very complex design in order to withstand the developing centrifugal forces.

The *patient table* is the component of the CT system on which the patient is placed. It is designed to withstand heavy weights without bending and is made out of materials that do not disturb the data acquisition outcome. The table is also a moving part of the CT system, since the patient has to be able to move in the z-axis during the scan and in the x-y axes before the scan in order to center the patient in the appropriate position.

2.3 Historic evolution of CT imaging systems

2.3.1 1st Generation

The first generation of CT scanners were equipped with an X-ray tube and pinhole collimator, in order to emit a very thin beam towards the body and the detectors. This geometry is generally referred to as *pencil beam*. A single detector collects the attenuated beam on the other side of the body. This system required the movement of the detector and the beam in a linear direction across the field of view (FOV) for each projection angle. Then a small rotation moved the FOV to another projection and the linear movement was repeated. This process was performed for 160 parallel rays across a 24cm FOV for 180 one degree rotations.[5]

Except from the very long time needed to perform such complex mechanical movements, the system also had to deal with the large differences in signal intensity in its detectors. Due to the movement of the same detector across the body, it had to be able to measure rays passing from thin and thick parts of the body. Due to its inability to handle such changes in signal, the body had to be placed into a water bag. For both reasons, the only body-part that could be imaged was the head.[5]

On the other hand its thin beam provided very little scattered X-ray intensities, leading to the best geometry in scatter rejection until today[5]. It's simple geometry also simplifies the reconstruction technique required[4].

2.3.2 2nd Generation

In the second generation of CT, the single detector was replaced by an array of detectors. The beam shape also changed into a fan beam with a relatively small opening of 10 degrees. In this way a single ray was able to send signal to the whole array of detectors, speeding up the process. However, due to the more complex beam geometry and the increased distortion due to scattered

radiation, the projections needed in order to achieve acceptable image quality had to increase as well. According to *Bushberg et. al.* the shortest scan time with a second generation scanner was 18 seconds per slice, which is 15 times faster than 1st generation scanners[5].

Due to the small detector array of approximately 30 detectors and the small fan opening, linear movement of the tube and the detector array was still necessary. Also, cranial imaging was still the only possible application, since the still long scanning times required complete lack of respiratory movement and immobilization of the imaged body.

2.3.3 3rd Generation

In the next generation of CT technology, effort was put into shortening scanning time. A scanning time of less than 20 seconds would allow scanning of the abdomen area[4]. Therefore the detector array was enlarged to about 800 detectors and the fan beam was greatly widened. This allowed the whole body to be imaged simultaneously, without the need of translational movement of the tube and detectors. This improvement was the key to shorter scanning times, as now only rotational movements were performed between different projections.

The most significant problem in 3rd generation scanners is the appearance of *ring artifacts* on the image. These artifacts are caused by miscalibrated or defected detectors. As each detector in the 3rd generation geometry is responsible for the collection of data corresponding to a ring in the image. Due to the rotation of the detectors, drift often causes signal shifting, leading to the ring artifacts.[4] [5]

2.3.4 4th Generation

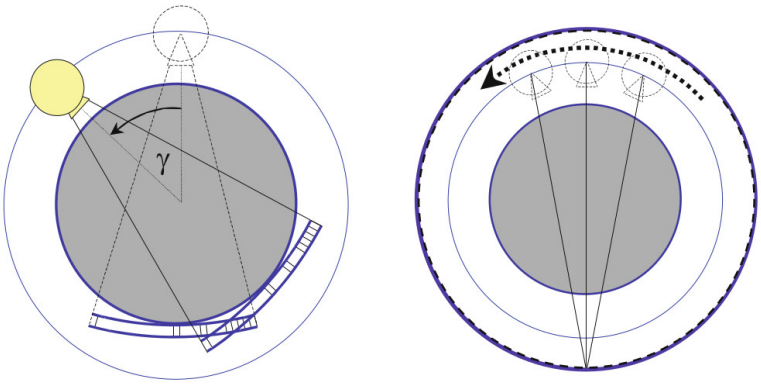

Figure 2.5: *left, 3rd Generation CT fan beam geometry. right, 4th Generation source fan geometry.*

The 4th generation of CT scanners came in an attempt to overcome the

ring artifacts problem. Since movement of the detectors was the source of the problem, stationary detectors were introduced. The moving ray of detectors was replaced by a ring of non moving detectors. Another difference is that the X-ray tube now moved continuously, in contrast with the previous generations where a step and shoot approach was used.

In this setup an inverse fan geometry is used. This means, that the acquired data is normalized during the scan so that the apex of the fan is an individual detector and the fan opens towards the moving tube. This means that while in previous generations fan data is acquired in one instance of a time from multiple detectors, now the fan data is acquired during the whole rotation of the tube from a single detector.

2.3.5 Electron Beam CT

In an attempt to construct a high speed CT system, the conventional X-ray tube was replaced by a stationary electron gun. The emitted electron beam was steered towards a large tungsten arc. The electron beam could electronically sweep along the tungsten target generating a moving fan like photon beam[13]. The photon beam looked towards a large arc of detectors (more than 180^o). The system lacked any kind of mechanical movement except from the slowly moving patient table. This system is called *Electron Beam CT* (EBCT).

The EBCT system (see Figure 2.6) was designed in order to produce high speed CT images (of 50 ms scan times). This allowed the imaging of the heart and the production of CT movies[5]. As the construction cost was much higher than other CT technologies and it's main advantage was its short scanning times, it was primarily used for cardiac imaging. Nowadays less costly CT technologies are also able to produce cardiac CT images.

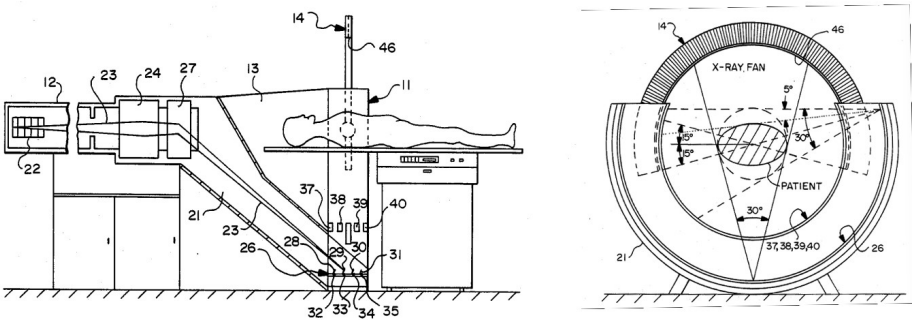

Figure 2.6: *Diagram of the Electron Beam CT system, as patented by Imatron.*[13]

2.3.6 Helical CT

The next big step in CT technology came with the incorporation of *slip ring* technology (see Figure 2.7). In 1st through 3rd generation CT systems, the moving detectors were restricted to 360 degree movements due to the limited length of the cables attached to the detectors. This obliged the detectors to move back to their starting point after every rotation. While this problem was earlier dealt by switching between clockwise and counterclockwise rotation, the system still could not develop high velocity due to the increasing torsional moment. The slip ring is a metal ring through which the energy or signal is transferred to the detectors by the means of sliding brush-like contacts. The slip ring allowed the free movement of the *gantry*, the moving part of the CT device, and much faster rotations, leading to shorter scanning times.

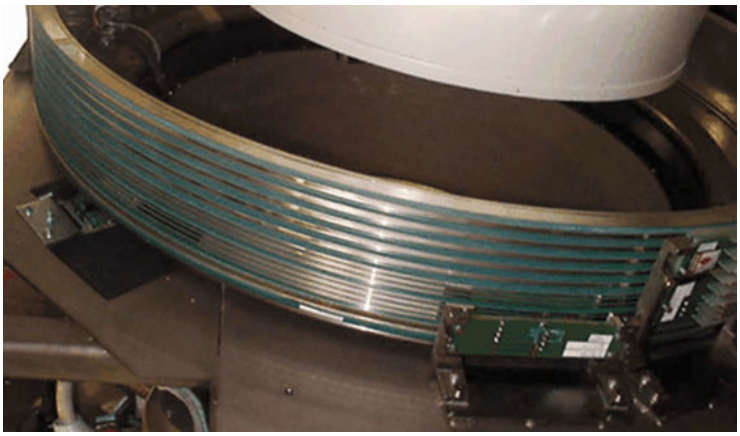

Figure 2.7: *Image showing the slip ring technology with the brush contacts sliding over the ring.*

With the free movement of the gantry the development of *Helical or Spiral CT's* is now possible. In helical CT scanners, the acquisition of data is no longer performed in two dimensions. The gantry now rotates while the patient table moves with constant speed, providing a helical acquisition geometry. The advantage of this acquisition technique is speed, since the start/stop motion of the table and the gantry in previous generations is now replaced by continuous movement. Altering the CT table's velocity, the scanning speed can change even more, at the image quality's expense. For helical CT, it is important to define the scan's *pitch*. The pitch of the helical scan is defined as

$$pitch = \frac{F_{table}}{nT} \tag{2.5}$$

where F_{table} is the the feed distance of the table for a complete circular gantry rotation and nT is the nominal collimated beam width[3]. For most helical CT scanners, the pitch can vary from 0.75 to 1.5. A high pitch value can be used

for thoracic scanning, where speed is important, or pediatric scanning, where lowering radiation dose is important. On the other hand, a low pitch value is used in cardiac imaging.

2.3.7 Multidetector CT

In the race for faster scanning times, CT developers started using multiple detector arrays. With the multiplication of detector arrays, the beam has to be widened as well, in a geometry called *cone beam geometry*. The use of multiple detector arrays leads to the acquisition of multiple slice data from a single rotation. Such CT systems are therefore called *Multidetector* or *Multislice* CT scanners (MDCT)[5][4]. The use of multiple detector arrays leads to the acquisition of multiple slice data from a single rotation.

When the CT system has many detector rows (> 64) and the cone angle is large enough, the reconstruction algorithm takes the angle into account. These systems are called *Cone Beam CT's*. They have the advantage to perform whole organ scans without the need of table movement, with applications such as CT Angiography and perfusion studies. Such wide cone beams have their disadvantages however, since the system has to deal with a large amount of scattered radiation and artifacts.[3]

The evolution of MDCT has been rapid in the early 21st century. From 4 arrays in 1998 we now have systems with 640 arrays of detectors (2014). The combination of multislice with helical CT is nowadays used extensively, leading to systems with very short scanning times and very good image resolution.

2.3.8 Dual Source CT

In 2006, Siemens released the first *dual source CT* system (DSCT) (see Figure 2.8). In this setup, two independent X-ray tubes and sets of detector arrays with an angular offset of 90 degrees are used[15]. Due to space limitations, the second array of detectors covers a smaller field than the first one.

The system was specially designed for cardiac imaging, in order to provide better temporal resolution than MDCT systems, but has also applications in general CT scanning[15]. The system allows the operation of the two tubes on different energies, allowing also dual energy scans (see 2.3.9).

2.3.9 Dual Energy CT

Since the acquired data in CT is the material's linear attenuation coefficient, materials of different elemental composition might produce the same HU in a CT scan. This can make it difficult to distinguish certain tissues from each other. The solution to this problem was found very early in CT's history by Hounsfield. In 1973 he found that iodine (z=53) and calcium(z=20), which showed similar HU's, could be differentiated with the use of two different beam energies. [12]

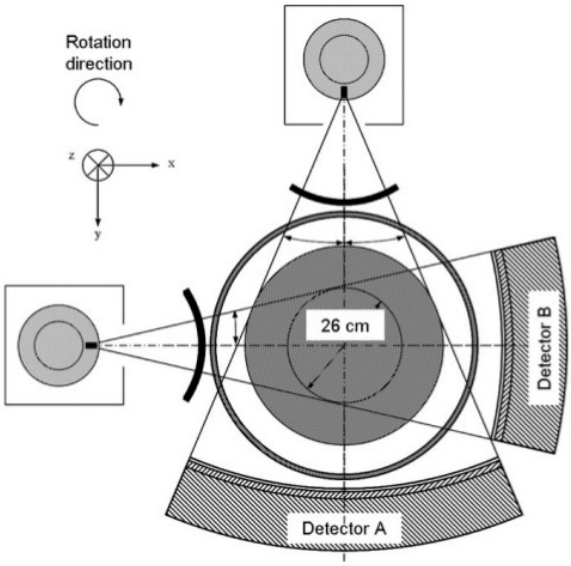

Figure 2.8: *Diagram of the first DSCT system.*[14]

There have been different approaches in dual-energy acquisitions. The first approach was with the use of two sequential scans, but patient motion during the scan lowered the quality of the outcome. The real breakthrough of dual energy CT came with the introduction of real-time or near real-time techniques.

In the 1980's a CT system with a tube that had the ability to rapidly switch between two different tube potentials appeared. This allowed for near-simultaneous data acquisition of the two energy datasets.[16]

Another mechanism is the use of multilayer detectors. A single high tube potential is used while the detection system consists of layered scintillation detectors. The detectors in the front layers collect the low-energy data while the high-energy data is collected by the back layer of detectors. The mechanism has the advantage of simultaneous data acquisition of the two different energies.[16]

Dual Energy acquisition has also been performed by the use of DSCT systems. This technique has the advantage that the two tubes are independent and that the spectral overlap of the energies is relatively low, compared to the other real-time techniques.

Energy-resolving photon counting detectors have also been proposed in dual energy CT, although no commercially available system has yet been released. These detectors have the ability to count each photons interactions, leading to a *multi energy CT* system, where the data can be divided in different energy windows.

2.4 CT hardware

2.4.1 X-ray Tube, Filtering and Collimation

The tubes used in contemporary CT devices are technologically advanced rotating anode tubes. They deliver high currents up to 1000mA and therefore have good thermal management (up to 8MHU thermal capacity and 4.7MHU/min thermal abduction). The latter allows the tube to operate through all the scanning period without the need to stop. The tube also has to withstand the mechanical stress induced on it during rotation. It therefore is resistant to up to 13G accelerations allowing very high rotation frequencies.

The low energies of the X-ray spectrum produced by the tube are not useful in CT imaging. They do not contribute to the image quality of the acquisition and are therefore filtered inside the tube for radiation protection reasons. The filter used is usually a flat or shaped aluminum filter.

After the filtering the beam is shaped accordingly. The beam first passes through a collimation system consisting out of moving lead foils. Then a *bow-tie filter* is used in order to shape the spatial distribution of the beam intensities. The bow-tie filter allows higher intensities through the central part of the beam and lower intensities through the outer parts of the beam, since the beam is going to attenuate more in the central part of the imaged body. Thus, it counterbalances the intensity differences due to different depth, delivering almost constant intensities to the detectors, regardless their spatial position.

After the beam passes through the patient, the beam is collimated again with what is called a *post patient collimator*. This collimator system is placed just before the detection system, shaping the nominal slice thickness of the fan beam.

2.4.2 Detectors and Arrays

A detector is described mainly by its ability to detect photons, generally referred to as *detection efficiency*. The detection efficiency of a detector is determined by its geometric efficiency mainly described by a parameter called *fill factor*, it's *capture efficiency* and it's *temporal efficiency*.

The geometric efficiency is better when the fill factor, meaning the percentage of its surface that is able to detect photons is higher. The capture efficiency is its ability to capture and convert photons into signal while the temporal efficiency is dependent on the *dead time* of the detector after a photon-detector interaction.

Here follows a description of the detectors and detection systems used in modern CT systems.

Xenon Gas Detector Array

The xenon detector array consists out of a chain of alternating anode and cathode pairs. Between them, there is xenon gas, responsible for the creation of pulses through the anode and cathode.

Xenon is a noble gas used as a detector. The photoelectric interaction

$$Xe + hv \rightarrow Xe^{+} + e^{-} \tag{2.6}$$

that occurs between a photon and xenon, is responsible for the release of electrons and positive xenon ions creating a chain reaction. These ions are absorbed through the cathodes while the electrons are absorbed through the anodes in the detection system of the CT and consequently pulses are created. These pulses are amplified and digitized in a measurement proportional to the x-ray intensity falling onto the detector.

Xenon has a relatively low capture efficiency. Therefore it is usually highly compressed in order to increase its interaction probability with the passing X-rays. Another method to combat this problem is the creation of long xenon chambers, in order to have longer travel times inside the xenon gas. The latter also improves the directional selectivity of the detector and the xenon detector is therefore considered highly directional.[5]

Solid State Scintillation Detectors

Solid state CT detectors consist out of a scintillator material in contact with a photodetecting diode (photodiode). The X-rays interact with the scintillator, producing long wave radiation (light). The long wave radiation is then converted into electric pulses through the photodiode. The photodiode has to be able to absorb photons in the same frequencies as the scintillator emits. Therefore photodiode-scintillator matching is very important in the creation of an efficient solid state detector.

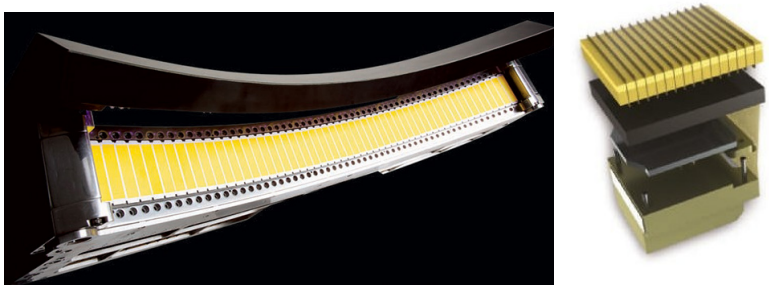

Figure 2.9: ***Left:*** *GE's Gemstone detector array. Courtesy: GE Healthcare.* ***Right:*** *The Philips NanoPanel Prism detectors on the IQon scanner. Courtesy: Philips Healthcare*

Typical scintillator materials used in CT are CsI (cesium iodide), BGO (bismuth germanate) and cadmium tungstate ($CdWO_4$). Because the density and atomic number of the solid state materials is much higher than in xenon gas, scintillator detectors have much higher capture efficiency. They also produce much less image noise.[17] On the drawbacks, solid state detectors have reduced

geometric efficiency. This is due to a small gap between neighboring detector elements, which is necessary in order to reduce crosstalk noise.

Solid state detectors have a wider range of photon detection angles. This means more scattered X-rays are detected, which is often undesirable. Therefore collimator lamella, known as *antiscatter grid*, are often attached between different detection elements, in order to get rid of high angle photons before they reach the scintillator. This greatly reduces noise levels, but decreases the total geometric efficiency of the detector.

Modern solid state CT detectors are manufactured in modules consisting out of several square or rectangle detector elements, separated with an opaque filler. These elements are in contact with the photodiodes and sit onto a stack of electronic modules responsible for power delivery and signal reception. Multiple detector array modules are mounted into an aluminum arc-shaped frame onto the gantry.

2.5 Reconstruction Methods

Each individual projection measurement corresponds to a measurement of an attenuated ray I_i. The purpose of the collection of this data is, as discussed, the analysis of the attenuation coefficients μ into the body of the patient. This analysis will result into a matrix of attenuation coefficients, after a reconstruction algorithm is applied.

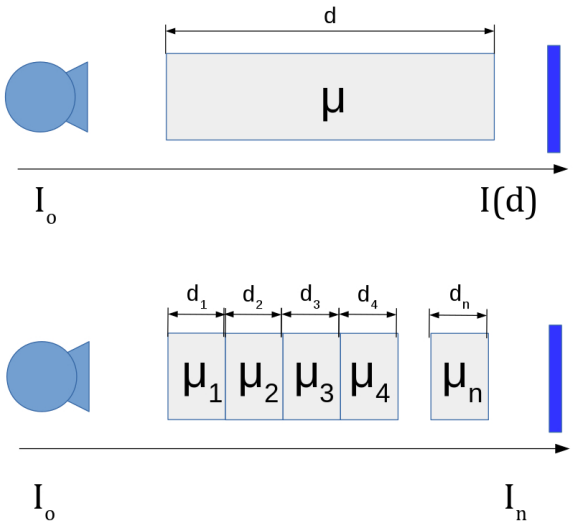

Figure 2.10: *Graphical representation of the difference between one homogeneous material and multiple different materials.*

When a photon beam is attenuated through a single homogeneous material (see figure 2.10, *top*), the calculation of the linear attenuation coefficient is through an easy transformation of equation 1.6, into

$$\mu = \frac{1}{d}\, ln \frac{I_o}{I(d)} \tag{2.7}$$

where d is the material thickness.

If we try to do the same in an inhomogeneous material with different attenuation coefficients like in figure 2.10, *bottom*, the problem becomes much harder to solve. For this reason CT acquires a large number of projections, in which we collect a number of equations in the form of equation 2.3, which need to be reconstructed into an attenuation coefficient matrix. The methods used in order to reconstruct the intensity data into attenuation data are described in this section.

2.5.1 Object Space, Radon Space and Fourier Space

In order to continue the analysis of the reconstruction process a brief introduction to the mathematical domains will be made.

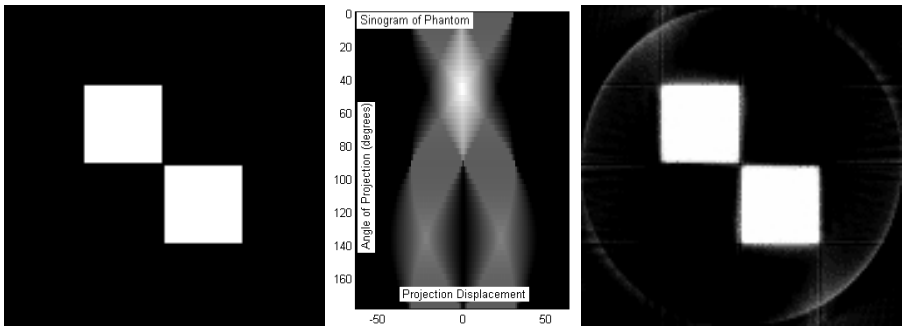

Figure 2.11: ***left:*** *Phantom object,* ***center:*** *Sinogram of the phantom object,* ***right:*** *Reconstructed image of the sinogram*

The *Object Space* is the physical Cartesian space of the imaged object. The data representing the image object is stored into a matrix of attenuation coefficients. The matrix cells represent the image pixels (or voxels in 3D).

The *Radon Space* or *Sinogram Space* (see Figure 2.11 *center*) is a space into which the projection values of each angle are stored. One specific projection angle represents one horizontal line in the image space. The transform function which leads to the Radon Space data is the *Radon Transform*. The Radon transform Rf, is a function defined on the space of straight lines L in $\Re^2$ by the line integral of function $f(\mathbf{r}) = f(x, y)$, which represents an unknown density:

$$Rf(L) = \int_L f(\mathbf{r})|d\mathbf{r}| \tag{2.8}$$

A 2D Fourier transform applied on the object space's data leads to the *Fourier Space*. The interrelation between the Fourier Transform and the Radon transform allows the creation of the Fourier space also by a 1D Fourier transform of the Radon space data. This is a consequence of the central slice theorem. According to this theorem, if we take a 2D function, project it onto a line and do a Fourier transform of that projection; we get the same outcome as when we perform a 2D Fourier transform first and then slice through its origin, which is parallel tho the projection line.

2.5.2 Simple Backprojection

The simplest way to visualize the data collected from a CT scan is through *backprojection* of the the transmission profiles from each angle. In each projection angle, the CT device detects and stores a transmission profile, which corresponds to the attenuation coefficients each detection element measures. This transmission profile is distributed evenly over the area it projects into the empty image matrix. In this way each attenuation coefficient corresponding to a single ray is added to the matrix cells through which the ray passes. The same is done for every other transmission profile collected. One over an other, the transmission profiles are distributed over the image matrix producing a final image which is very blurry but does depict the scanned body.

The blurriness is a result of the 1/r radiation of a radiated object[5]. An object will contribute to the attenuation coefficient of a matrix cell, even if it is not inside that cell. This contribution has a dependency of 1/r, where r is the distance between the object and the point of measurement. In order to overcome the blurriness of the simple backprojection, the transmission profiles can be filtered. The addition of this step in the reconstruction process is called *filtered back projection*, and is the most common reconstruction technique in modern CT systems.

2.5.3 Filtered Backprojection

Filtered backprojection is performed into four mathematical operation steps. The Acquired data is received in the form of a radon space matrix. A 1D Fourier transform is applied onto the received matrix converting the data into Fourier space. Then a filter is applied to the Fourier space data and an inverse Fourier transform is applied to the filtered data, converting it back into Radon space. After that, backprojection of the Radon space into the object space produces the reconstructed image.

The filter that is applied into the Fourier space can also be replaced by a direct application of an appropriate kernel onto the projected data, according to the convolution theorem for Fourier transforms. If the collected data is expressed as the projection $p(t, \theta)$, where t is the displacement from the isocenter of the projection and θ is the projection angle, then equations

$$p'(t, \theta) = p(t, \theta) \otimes k \tag{2.9}$$

and

$$p'(t,\theta) = FT^{-1}\{FT[p(t,\theta)] \times K\} \tag{2.10}$$

are equal if $K = FT[k]$. This means that the convolution of kernel k with the projection data is equal to the inverse Fourier transform of the projection data multiplied with the Fourier transform of the k kernel.

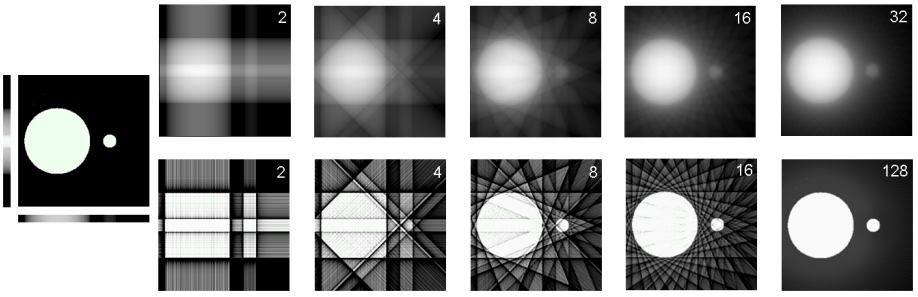

Figure 2.12: *Reconstruction of a phantom (left) through simple backprojection (top) and filtered backprojection (bottom). The number in the top-right corner of each reconstruction represents the number of used projection angles.*

Various filter types are available, all emphasizing on different characteristics of the CT image. Typical filter types are bone filters and soft tissue filters; also called sharp and smooth filters respectively. The sharp filters allow higher frequency depiction and better resolution, but produce more image noise. The smooth filters produce images with higher contrast and less noise. The latter are thus more suitable for soft tissue.

2.5.4 Algebraic and Iterative Reconstruction Techniques

Algebraic reconstruction techniques refer to reconstruction through equation solving. Due to the large data that has to be managed, such techniques are impractical, time consuming and are thus not used in commercial CT devices. Other problems concerning algebraic reconstruction techniques are sensitivity to stochastic noise and susceptibility to measurement errors.

Iterative reconstruction techniques are based on optimization processes, in which algorithms try to find the best matching image to the collected data. They were widely used in early CT history but vanished later on; with filtered backprojection dominating over all other reconstruction techniques. The increase in computational power although reignited interest in these reconstruction techniques and are nowadays used even in commercial systems.

Iterative reconstruction techniques are often used in combination with backprojection techniques. Although the techniques used are patented, it is known that they are used for noise removal. Iterative reconstruction algorithms are classified according to the data on which they are applied, with algorithms both for raw data and image data being available by all major CT manufacturers.

The major advantage of iterative reconstruction techniques is their ability to produce good quality images with lower patient doses, through noise removal. On the other hand, increased reconstruction time is needed, making such processes impractical for emergency cases.

Chapter 3

Heart Anatomy, Physiology and Pathology

3.1 Basic Heart Anatomy and Physiology

The heart is a muscular organ serving as a pump for the circulatory system. It pumps blood through the vessels (arteries and veins) across the human body.

The human heart is positioned behind the sternum, in a region called mediastinum, between the two lungs directly above the diaphraghm, with it's top leaning towards the left and has a size similar to a male fist. It lies into a sac called the *pericardium*. The heart itself has four distinct cavities; the *right atrium* (RA), the *right ventricle* (RV), the *left ventricle* (LV) and the *left atrium* (LA). The outer wall of the heart has three layers; the inner *endocardium*, the intermediate *myocardium* and outer *epicardium*.[18]

The heart receives deoxygenated blood from two veins called *superior and inferior vena cava* both of which lead into the right atrium. The blood then passes through to the right ventricle through a valve called *tricuspid valve*. The blood is then pumped towards the pulmonary artery, which leads towards the lungs, through another valve called the *pulmonary valve*. The newly oxygenated blood flows back to the heart's left atrium through four pulmonary veins. Consequently, it flows into the left ventricle through a valve called the *mitral valve*. From there it is pumped towards the *aorta* (the main artery) through a valve called *aortic valve*. The aorta[1] leads towards the the lower body, with the upper body being supplied with four arteries which start at the arch of the aorta.[18]

In order to pump blood through the whole body the heart has to pump the blood with high pressure towards the aorta. Therefore the wall around the left ventricle is thicker and the aorta is around 4 cm wide. The pumping is achieved

[1]The aorta leaves the heart upwards, shaping the *ascending aorta*. After about 6 cm the aorta makes a turn 180 degrees downwards. The turn is called *arch of the aorta*. The rest of the aorta has a downward direction and is therefore called *descending aorta*.

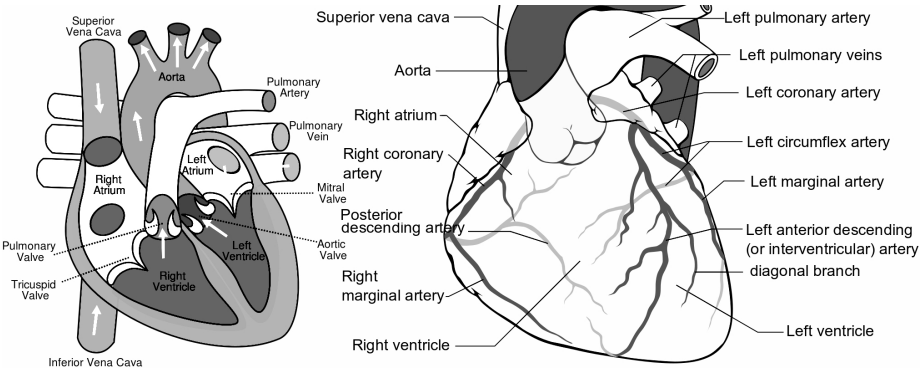

Figure 3.1: *Graphical representation of the heart.* ***left****: Interior view of the heart.* ***right****: Anterior view of the heart.*

through a strong contraction of the wall's muscle (myocardium) around the ventricles. The cardiac muscle cells are ordered in tightly bound layers (fibers), which completely encircle the blood chambers into the heart. When the wall contracts, the cardiac muscle cells band together, reducing the chamber volume and pressuring the blood towards the chamber exit.

The heart is, in practice, a double pump, since two consecutive contractions occur; a contraction of the atria and a contraction of the ventricles. In order for the contraction to take place, around one percent of the myocardial fibers have special features in order to be able to stimulate the heart. These fibers form the conduction system of the heart, which communicates with the rest of the myocardial fibers[19]. The conduction system is responsible for the start of the cardiac conduction and the fast spreading of the stimulation.

The initial stimulation of the myocardium comes out of a small group of myocardial cells, known as the *sinoatrial node* (SA node). The SA node possesses the feature of automatic depolarization and repolarization and is therefore actually the pacemaker of the heart. It is positioned in the myocardium of the RA of the heart, near the entrance of the superior vena cava. From there the stimulation is delivered to the whole myocardium. First it spreads almost simultaneously in the RA and LA. After that the stimulation is delivered to the RV and LV through a part of the conduction system called *atrioventricular node* (AV node). The AV node lies at the base of the RA and delays the stimulation of the RV and LV for approximately 0.1 seconds. The connection between the two ventricles happens through the *bundle of His* and concludes in the *Punkinje fibers* who deliver the stimulation to all the lower myocardial cells, provoking both ventricles to contract.[18]

3.2 Coronary Circulation

At the base of the aorta, just above the aortic valve, arise two arteries responsible for the blood supply of the heart. The two arteries are called *right coronary artery* (RCA) and *left coronary artery* (LCA), arising from the right and the left respectively. [18]

The LCA starts as a single artery (left mainstream) and splits to form the *left anterior descending artery* (LAD) and the *left circumflex artery* (LCx). The LAD moves downwards in the anterior part of the heart forming branches and finally communicates with the posterior descending artery (see RCA branches). On its way it supplies the wall separating the two ventricles, the apex and the the anterior walls of the ventricles. The LCx supplies the posterior parts of the LA and upper LV. It has a main part called *left marginal artery* (LMA) and in some cases communicates with the RCA.[18]

The RCA starts at the right part of the aortic base shaping major branches. A major branch is the *posterior descending artery* (PDA), which supplies the wall between the ventricles and the atrioventricular node. Other important branches are the *nodal artery*, which supplies the right atrium and the sinoatrial node, and the *right marginal artery*, which supplies a part of the right ventricle, a portion of the inferior left ventricular wall and the PDA. The RCA is in most cases responsible for the blood supply of the wall between the atria and the ventricles.[18]

The coronary artery description is the basic view of the coronary circulation, although variation exist. The left and right coronary arteries occasionally arise by a common base. In other cases their number may increase to three, with an additional posterior coronary artery, smaller in size. It also might be that a coronary artery is replaced by two arteries parallel to each other.

The artery supplying the PDA determines the coronary artery dominance. If the PDA is supplied by the RCA, the coronary circulation is right dominant (60-65% of cases)[18]. If on the other hand the RCx supplies the PDA, then the coronary circulation is left dominant(10-15% of cases)[18]. It might also be the RCA is supplied by both RCA and RCx. Then it is co-dominant or balanced. The coronary artery dominance influences artery diameters [20] and blood flow inside the arteries. Normal coronary artery diameters can be seen in table 3.1.

Location	**Normal Men**		**Normal Women**	
	n	Diameter (mm)	n	Diameter (mm)
RCA middle	20	3.9 ± 0.6	10	3.3 ± 0.6
LCA middle	18	4.5 ± 0.5	10	3.9 ± 0.4
LAD middle	20	3.6 ± 0.5	10	3.2 ± 0.5
LCx middle	20	3.4 ± 0.5	10	2.9 ± 0.6

Table 3.1: Lumen diameters of coronary arteries in normal men and women, as measured by Dodge et al.[20]

The venous circulation of the heart is mainly performed through the coronary sinus. The coronary sinus is a collection of veins returning from the myocardium that come together forming a large vessel that delivers deoxygenated blood to the RA. It is positioned in the posterior part of the heart. In the anterior part of the heart, lesser veins end up in a large vein, the great cardiac vein, that leads the deoxygenated blood towards the coronary sinus.[18]

3.3 Cardiac Electrophysiology and the Electrocardiogram (ECG)

As discussed, the stimulation of the heart begins in the SA node. The SA node is consists out of cells that have the potential to automatically generate pulses through depolarization and repolarization of the cells. These processes are related to the concentration of K^+, Ca^{2+}, Cl^- and Na^+ ions inside the membrane of the cells and are generated by their movement in and out of the cell. The exchange happens through specialized proteins called ion channels. The change in action potential in the SA node cells triggers the change of potential in normal myocardial cells which in turn trigger their neighboring cells. Thus, the whole heart gets triggered, causing myocardial systole or diastole, according to the cell potential.[18]

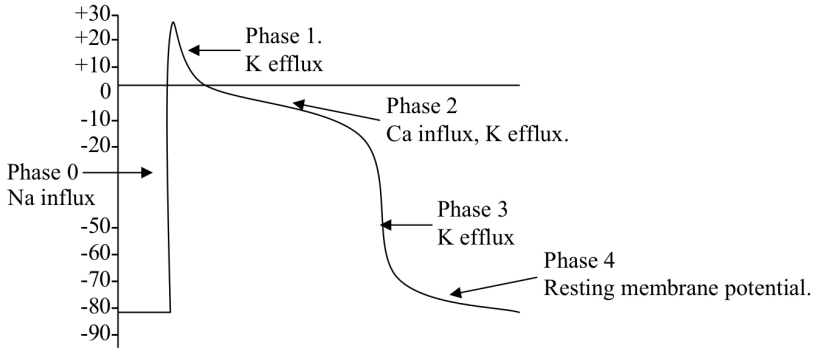

Figure 3.2: *Heart potential diagram*

A typical action potential wave of myocardial cells is illustrated in figure 3.2. Here we can distinguish five different phases which are known as phase 4, 0, 1, 2 and 3. Phase 4 is the stable state of the myocardial cell. In this phase no alterations in action potential take place. This changes with the transition to phase 0, where an influx of Na^+ triggers the action potential of the cell to rapidly move from -80mV to +30mV. A K^+ efflux stops this rapid depolarization transitioning to phase 1 of the action potential cycle. The cell starts repolarization due to this efflux. A Ca^{2+} influx slows this repolarization pro-

cess down, leading to a more stable phase 2, also called plateau. The Ca^{2+} influx however stops after a while, allowing again the repolarization process (now called phase 3) to take place. This leads the cell to again reach -80mV in what is called phase 4.[18]

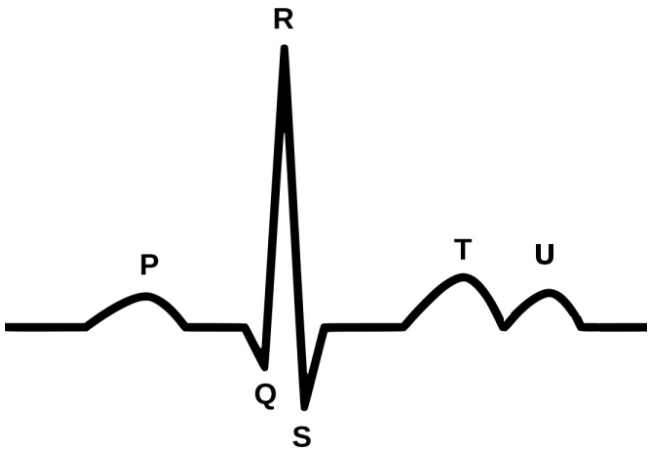

Figure 3.3: *Electrocardiogram*

The electrophysiology of the heart can macroscopically be monitored through the *electrocardiogram* (ECG). In an ECG, electrodes are placed on the skin and detect pulses caused by the cardiac cells. A healthy heart produces ECG pulses as visualized in figure 3.3. The ECG produces a group of waves labeled as P, QRS, T and U, each of which represent different heart activities. The P wave is the first wave and represents the depolarization of the atria. The QRS Complex is a group of three deflections which combined represent the depolarization of the ventricles. It is the highest of all other waves in the ECG. The T wave represents the rapid repolarization of the ventricle while the U wave that follows is much smaller and the source of it remains unknown.[21]

3.4 Coronary Artery Disease

Cardiovascular disease (CVD) is the group of diseases involving the heart and the blood vessels. CVD is the major cause of death world wide[22] and in Europe is responsible for 46% out of all deaths[23]. Out of these 46%, 20% of deaths are caused by coronary artery disease, 10% are caused by cerebrovascular disease and 12% are due to other cardiovascular diseases[23].

Coronary artery disease (CAD), is the group of diseases which affect the heart's coronary arteries. It includes both chronic phases of the disease, as well as acute syndromes (ACS) [24]; namely, stable angina, unstable angina, nonfatal myocardial infarction, and coronary death [25]. Common symptoms are chest pain and heartburn, while usually the symptoms are temporal and

occur while in physical or emotional stress. Major risk factors are high blood pressure, high cholesterol levels, smoking, poor diet, lack of physical activity, diabetes, advancing age and genetic disposition [22].

The underlying mechanism of CAD involves *atherosclerosis* (see Figure 3.4) of the coronary arteries[26]. Atherosclerosis is currently viewed as an inflammatory disorder [24]. It affects the endothelium of medium to large blood vessels when exposed to high levels of low-density LDL cholesterol, free radicals and other substances, by becoming transparent to monocytes and lymphocytes. When these cells are allowed through the endothelium of a vessel, they migrate to the inner layers of the vessel wall, attracting LDL cholesterol proteins into the wall forming macrophage cells. This allows the formation of a fibrous cap consisting of smooth muscle and collagen around the macrophages.[26] As the lesion progresses, mechanisms similar to those in bone formation may develop, causing calcification[24]. The macrophage cells eventually start dying under the fibrous cap, forming the so called atheromatous plaque[26].

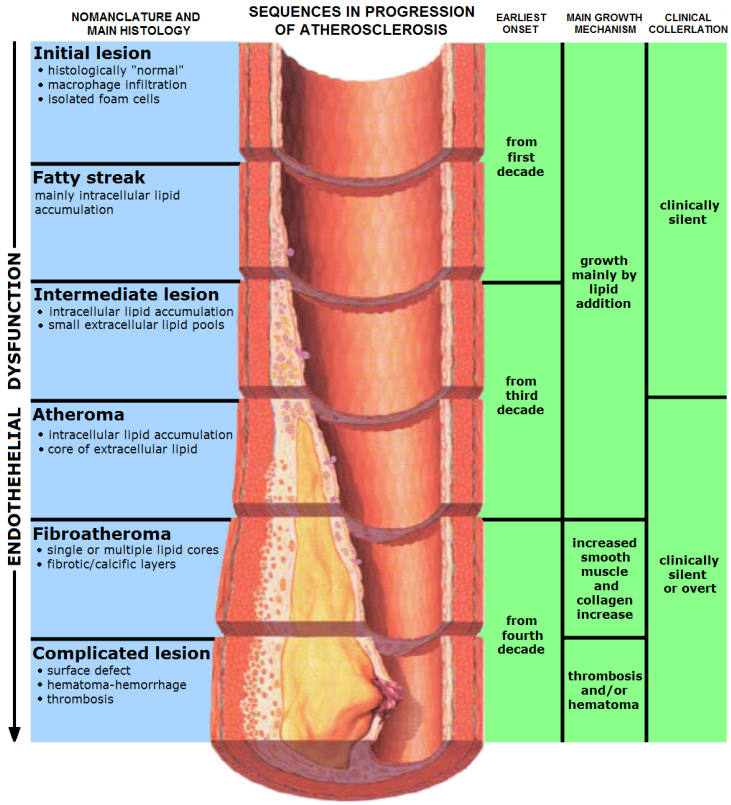

Figure 3.4: *Stages and progression of atherosclerosis*

Atheromatous plaques cause the artery's soft lining to become hardened, inelastic and swollen, with calcium and fatty deposits, and abnormal inflam-

matory cells [24]. They have the tendency to enlarge over time; as cells and lipids accumulate in them, swelling either outwards (nonstenotic) or inwards (stenotic) the vessel lumen [24]. The swelling causes thinning of the fibrous cap, which may crack, allowing fragments to be released into the vessel lumen. The released fragments result into the formation of thrombi; which, if large enough, may block the blood flow in the vessel resulting in a heart attack or a stroke.[26] Stenotic lesions tend to have smaller lipid cores, more fibrosis and calcification, thick fibrous caps and less enlargement. On the other hand, nonstenotic lesions tend to have larger lipid cores and thinner fibrous caps, which are more susceptible to rupture and thrombosis. Nonstenotic plaques may cause no symptoms for many years, but when they become disrupted, they can provoke episodes of unstable angina or myocardial infraction.[24]

Chapter 4

Cardiac CT

Cardiac computed tomography is the imaging through CT of the heart. The main issues in heart imaging are the fast movement of the heart due to it's beating, as well as it's relatively small structures that are of interest (such as the coronary arteries, which move several times their diameter during each heart beat). Therefore Cardiac CT is an application that requires high temporal as well as high spatial resolution at the same time[27]. Current conventional scanners used for cardiac imaging employ either MDCT, or EBCT techniques. EBCT allows for high resolution imaging at 50-100 ms while MDCT, with improved spatial resolution, allows for rotation speeds of 260-350 ms. Contemporary CT has the ability to image in submillimeter slices, providing high z-axis resolution, which is crucial in Cardiac CT (as will be explained later). In-plane resolution is dependent upon the number of pixels that can be produced by a given detector array. Resolution of current CT systems uses a matrix of 512×512, allowing x and y axis resolution down to 0.35 mm. This allows the current CT systems to produce nearly cubic voxels, enabling volumetric imaging.[27]

Although cardiac CT is performed both by EBCT and MDCT, the higher versatility and lower cost of MDCT has made the latter the leading CT modality used in cardiac CT. Therefore we will proceed the discussion of cardiac CT based on MDCT.

4.1 Techniques and settings used in Cardiac CT

4.1.1 ECG Gating

In order to image the entire heart using current CT systems, cardiac gating techniques are required (ECG gating). With these techniques, CT reconstruction uses data acquired over several heart cycles and during specific phases of the cardiac cycle. There are two methods of ECG gating employed in Cardiac CT, namely Retrospective and Prospective ECG Gating.[3]

Retrospective ECG Gating involves a continuous spiral feed and scan, a CT image is reconstructed using only a part of the collected data. The parts that are chosen for reconstruction are those taken while at a relatively stationary phase of the heart cycle.[3] [27] Irregular heart rate, however, can make the gating process challenging. Therefore Beta Blockers are often provided to patients with irregular heart rate, in order to enhance the imaging process.

Prospective ECG Gating (also called *step-and-shoot*) relies on the scanner initiating imaging only during a pre-specified interval of the cardiac cycle (usually the end-diastolic period of the cardiac cycle).[3] [27] With this gating method the radiation dose to the patient is significantly reduced compared to retrospective gating. On the other hand, due to the small capturing time during each heart cycle, if the patient's heart beats irregularly during the scan, the acquisition may lead to a broken dataset.[3]

4.1.2 Tube Voltage

As mentioned, cardiac CT requires besides high spatial resolution, high image quality, in order to visualize the small structures that are of interest in cardiac imaging. The tube voltage in cardiac CT had therefore not changed in cardiac CT for the first two decades of use, staying at 120kV for MDCT and 130kV for EBCT. But in recent years, with better imaging techniques, lower voltage protocols have been tried out[28] [27] [29], since reducing the kV, exponential reduction in radiation doses can be achieved. But since kV reduction increases noise levels, these approaches are only applied on thinner patients. Increasingly 100 kV and 80 kV studies are being reported, especially in children, where low radiation levels are more important.[27]

However, the kV reduction is more difficult in calcium scoring[29] for the following reasons. Firstly, due to the low radiation doses in calcium scoring imaging. Secondly, as the kV is lowered, calcium and contrast appear brighter, and this would change the calcium scores, which up until this point, have only been obtained using 120 kV acquisitions (and 130 kV for EBCT), requiring recalibration of the scoring algorithms.

4.1.3 Isotropic Data Acquisition

The most important advance in new MDCT systems, is the reduction of slice thickness. This is important for the improvement of image quality. Since slice thickness has evolved to as little as 0.5 mm, voxel dimensions are becoming nearly isotropic. Thus no data is lost by reconstructing the image in a different plane. This is important in coronary, peripheral and carotid artery imaging, since they run vertically to the imaging plane (z-axis). In addition, thinner slice imaging allows for less partial volume artifacts and less shadowing from dense calcifications and metal objects, which are common in cardiac imaging.[27]

4.1.4 Field of View

Image quality in cardiac CT can be improved by keeping the field of view (FOV) small. This allows the CT matrix (512×512) to cover a smaller area, increasing spatial resolution. This simple method of improving spatial resolution can easily be applied to cardiac CT, since it covers only a diameter of 15 mm.[27]

4.1.5 Halfscan Reconstruction

In cardiac CT, the most common reconstruction algorithm employed, uses (theoretically) data from a 180 degree gantry rotation. This is called *halfscan reconstruction*. Technically, 180 degrees plus the fan beam width are required for a halfscan reconstruction. This reconstruction technique improves the temporal resolution of the system, almost halving the time needed in order to acquire the needed data for a single slice reconstruction.[27]

4.1.6 Multisegment Reconstruction

Another reconstruction technique used in cardiac CT is *multisegment reconstruction*. Instead of acquiring the needed data for the reconstruction of one slice in a single heart beat, the reconstruction algorithm uses segments (typically 2-4 segments) from consecutive heartbeats in order to simulate a halfscan rotation. The technique uses a helical scanning technique, together with ECG synchronization. Images are retrospectiely aligned to the ECG data acquired, in order to keep track of the cardiac phase.[27]

The use of multisegment reconstruction has allowed for markedly improved effective temporal resolution and image quality. Although, the difficulty in using this technique is that the different segments must align properly. Patients with even very slight arrhythmias, changing heart rates, or premature beats may cause misregistration.[27]

4.2 Clinical Applications

According to the American College of Radiology, Cardiac CT's primary clinical use is for the morphological evaluation of the cardiac chambers, valves, ventricular myocardium, coronary arteries and veins, aortic root, central pulmonary arteries and veins, and pericardium.[30]

Cardiac CT delivers several diagnostic capabilities related to Coronary Artery Disease. Non contrast enhanced studies can reveal calcified lesions in vessels of the heart and its periphery, and are performed mainly for this cause[30]. Algorithms have been developed to quantify the calcification in the cardiac vessels, categorizing the severity of the atherosclerotic process. Another clinical use is for cardiac surgical planning in reoperative patients[30].

Cardiac CT can also be performed in parallel with intravenous administration of iodinated contrast.Through contrast enhanced studies, one can identify ventricular volumes, and observe wall thickening and motion accurately[27].

Specifically, contrast visualizes the cardiac chambers, the myocardium, the valves, the pericardium, and central great vessels [30]. Through CT coronary arteriography, the path of the coronary arteries is clearly visualized, while at the same time stenosis, aneurysm, and atherosclerotic plaque is revealed[30].

Three dimensional CT angiography is developing, allowing a more accurate view on the coronary arteries than with traditional two dimensional fluoroscopic angiography. CT angiography has the ability to overcome fluoroscopic angiography's limitations such as its inability to see beyond the lumen, visualizing both the lumen and the wall's composition, as it recognises fat, calcium and fibrous tissue. It also offers the ability to quantify information, enhancing the diagnosis of CAD. Soft plaque evaluation may prove to have prognostic significance over coronary calcium or risk factors alone, as well as helping to target revascularization.[27]

4.3 Coronary Arteries Calcium Scoring

As discussed in the previous chapter (see 3.4), atherosclerosis of the coronary arteries develops calcifications over time. These calcified lesions are visible on non enhanced cardiac CT (see 4.2). With the introduction of cardiac CT in the 1980's, the ability to quantify imaged cardiac data first appeared. This led to the introduction of algorithms that tried to quantify the calcifications present in the coronary arteries. The first attempt was made by Agatston and Janowitz in 1990[31]. They proposed a semiquantitative algorithm for CAC scoring, which later was named *Agatston Score* (or *AJ Score*, or simply *AS*) becoming the gold standard for calcium scoring until today.

CAC scoring has been linked strongly to incident CHD and death, providing incremental predictive information beyond that provided by standard risk factors [32]. Generally it has been shown that higher CAC scores represent more severe CAD and therefore the outcomes have been sorted into categories, representing the severity of the atheroscleroc process and the probability of significant CAD and CV implications [33].

4.3.1 Agatston Score

The scoring algorithm proposed by Agatston and Janowitz was originally intended for an EBCT scanner, producing 3 mm slices taken at 130kV[31]. Although equivalent scoring algorithms have been developed for MDCT scanner images of various slice thickness, taken both with retrospective and prospective scanning, using 120kV. Studies reported very few differences between the two different scanners and their protocols [34].

Every lesion on a single slice with an attenuation threshold of 130 HU and an area of at least 1 mm^2, is scored based on its covered area, and multiplied by a density factor. Since a CT image slice consists out of pixels, the area of the lesion is calculated as the number of pixels multiplied by the corresponding area covered by a single pixel. The density factor is based on the

maximum HU inside the lesion on a single slice. It has four steps, as seen in table 4.1, so that regions with higher CT number, and thus higher calcium density, contribute more strongly to the final calcium score. The total AS, is thus calculated as the number of pixels exceeding the 130 HU threshold, multiplied by the corresponding pixel area, multiplied by their density factor. [31]

Density factor	Max. HU
1	130-199
2	200-299
3	300-399
4	≥ 400

Table 4.1: *The density factor takes its value from the maximum HU detected into the area of each calcification*

The Agatston score has extensively been used in clinical practice, having positive predictive value to CAD severeness and risk of acute CV events. Therefore guidelines have been suggested to categorize AS scores. Such a guideline is shown in table 4.2.

Agatston Score	Plaque burden	Probability of significant CAD	Risk of CV implications
0	No identifiable plaque	Very low, $< 5\%$	Very low
1-10	Minimal identifiable plaque burden	Very Unlikely, $< 10\%$	Low
11-100	Definite, at least mild atherosclerotic plaque burden	Mild or minimal coronary stenoses likely	Moderate
101-400	Definite, at least moderate atherosclerotic plaque burden	Nonobstructive CAD highly likely, obstructive disease possible	Moderately high
> 400	Extensive atherosclerotic plaque burden	$> 90\%$ likelihood of at least one significant stenosis	High

Table 4.2: *AS categories according to plaque burden, probability of significant CAD and risk of acute CV implications[33]*

4.3.2 Calcium Volume Score

Some drawbacks of the AS are its stepwise stratification due to the nature of its weight factor, the fact that it does not represent a physical quantity and its limited reproducibility[35]. These considerations led to the development of the *Calcium volume score*, *CVS*.

The CVS is an isotropic interpolation method of calculating the volume of calcified lesions. The algorithm, as in AS, defines the calcified plaques as pixels with a minimum attenuation of 130 HU. In order to relate to the AS, the CVS is represented as a whole number, actual being measured volume in cm^3, multiplied by 1000.[35] Although the CVS represents a volume, it should not be considered as the actual calcified volume, since it still remains a scoring method. The actual CT numbers, do not contribute to the CVS calculation, serving only in the threshold definition.

4.3.3 Calcium Mass Score

The best attempt to get a scoring system that has actual physical value is the *Calcium Mass Score*, *CMS*. This method aims to measure the true calcium mineral mass of the lesion. It uses a heart phantom containing hydroxyapatite (HA) cylinders of known concentration in order to get calibration factors that relate the CT numbers with calcium mass [36].

The algorithm first calculates the calcium concentration as the mean CT attenuation for all voxels in a calcified lesion. Then it derives the mean calcium concentration from the association between the calculated mean attenuation and the calcium concentration in the calibration phantom. To calculate the mineral mass per plaque, the calcium concentration is multiplied by the volume of the calcified plaque. The total mass score is then the sum of all calcified plaques.[36]

The general equation for CMS calculation is

$$CMS = c/250 \cdot area \cdot section\ increment \cdot mean\ attenuation\ value \tag{4.1}$$

where c represents the calibration factor. The calibration factor is calculated based on the calibration phantom as

$$c = \rho_{CaHA}/HU_{CaHA} - HU_{water} \tag{4.2}$$

where ρ_{CaHA} is the real phantom density, while HU_{CaHA} and HU_{water} represent the mean HU values inside the plaque region and in water.[36]

Although the CMS delivers much lower variability than AS [37], having technical advantages, it has not been widely used in clinic and research [38].

4.3.4 Calcium Density Score

It has been suggested that high calcium density in plaques is associated with lower risk for acute CV events, since denser calcifications are observed in

stable CHD.[39] A calcium density score has therefore been developed and has acquired increased attention [38], since it has been shown to have significant inverse association with CHD and CVD risk [39].

The *Calcium Density Score* (CDS) is calculated with the help of AS and CVS. The CVS divided by the slice thickness yields the total area of calcium detected on all slices. The AS represents an area multiplied by the density factor. Thus, multiplying the AS by the slice thickness and dividing by the CVS,

$$CDS = \frac{AS}{CVS/slice\ thickness} \tag{4.3}$$

an average density score is recovered.[38]

Part II

Special Part

Chapter 5

Purpose

The purpose of this study was to determine the effect of patient heart rate during the cardiac CT imaging onto the CAC score estimated using acquired CT image data. The heart rate of a patient, is known to be a burdening factor in the image quality of cardiac CT examination. On the other hand CT systems with fast rotation times and broader detector arrays have the ability to tackle these problems and produce diagnostic images even at high HR levels. The calcium scoring however should probably still be influenced by the change in heart rate.

An in vivo study would require unjustified exposure to radiation for the patients, since a lot of images should be acquired from the same heart, at different heart rates. Furthermore, the use of real patients would require a method of altering the heart rate of the patient, something that could prove quite difficult. On the other hand, the medical physics laboratory has a 3D heart movement simulating phantom at its disposal. This aperture is ideal for the study of heart properties at different heart rates, since the same object can be imaged multiple times at a broad spectrum of different speeds.

Since calcified lesion phantoms were not available, the construction of this phantom was also a part of this study. The first step was the search of a calcified plaque equivalent material. Thereafter the shape and size were studied and constructed. The final lesion phantoms were made in such a manner that allowed the study of calcium scoring behavior in different sizes and concentrations.

The effects of heart rate on calcium studies have already been studied, on EBCT, DSCT and MDCT imaging systems. However, many phantom studies are with equipment able to simulate only 1D cardiac movement. Our purpose was to repeat and validate the research outcomes of these studies with a 3D simulation of heart movement, in order to better understand calcium scoring outcomes.

Chapter 6

Materials and Methods

6.1 CT specifications

The available CT system is GE's 64-slice Revolution HD®. The CT has spectral imaging capabilities, since it uses a kVp switching tube and gemstone® scintillator detectors. The tube has the ability to shift between 80 and 140kVp. The gemstone® detectors provide high definition imaging of 0.23 mm spatial resolution, while delivering a high temporal resolution. The system as a whole delivers 29 msec temporal resolution while being able to expand to a 50 cm FOV. As for the reconstruction, it uses the ASiR® and Veo® iterative reconstruction algorithms.

6.2 CAC scoring software and protocol

The calcium scoring software used in this study was GE's Smartscore® 4.0, which runs on the GE Advantage Workstation Server®. The Smartscore software measures AS, CVS and CMS. According to the software manufacturer, for optimum results heart rate should not exceed 80 bpm, as higher heart rate should result in increased blurring and artifacts.

The recommended protocol, in combination with the CT scanner is as follows:

- kVp: 120
- ma: SmartmA 50-430
- Avg mA: 300
- Scan type: Cardiac
- ASiR-v: 50
- Rotation: 0.28s

- DFOV: 25cm
- Thickness: 2.5mm
- AEC CACS Auto Gating profile
- Collimation: 140mm
- smartmA NI: 20 HU
- SFOV: Cardiac Large

As can be seen, the software uses 120kV images, as is standard in MDCT CAC scoring, with automatic mA selection. It proposes a 25 cm FOV in order to maximize spatial resolution while still holding the whole heart into the image. The slices are set at a 2.5 mm slice thickness, while employing a specialized prospective ECG gated scanning modality.

The Smartscore software offers semi-automatic calcium scoring. It automatically detects lesions by the pixel's HU value. The user has to validate the software's detection as a lesion in order to add the value to the total score. This is visually done, by selecting the highlighted lesion. The software also allows the categorization of lesions. For example, one can store the detected calcifications on different coronary arteries separately and review how much of the total score corresponds to each artery.

6.3 Cardiac Phantom and Motion Profiles

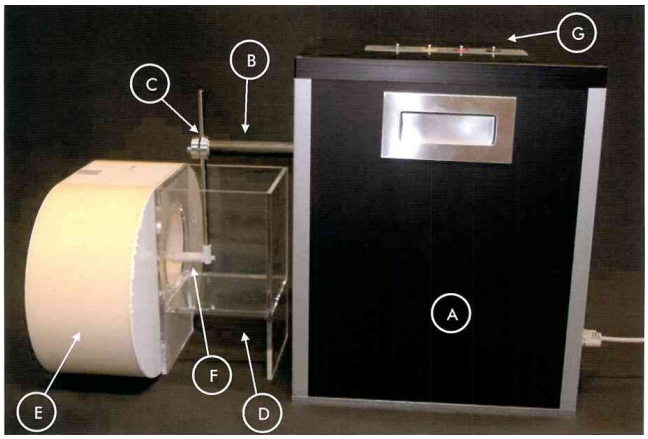

Figure 6.1: *The Sim4Dcardio© cardiac motion simulator, together with the anthropomorphic thorax phantom.*

The cardiac phantom used in this study was the Sim4DCardio© (QRM, Moehrendorf, Germany) dynamic phantom (see Figure 6.1).[40] This system has

the ability to oscillate small cardiac phantoms into a water tank (D), producing realistic simulations of heart movement. A phantom object (F) can be positioned onto a clamp (C), that is supported onto a carbon rod (B) that has the ability to produce small range 3D motion trajectories.

In order to achieve a realistic environment for the dynamic motion the water tank fits into a static thorax phantom (QRM, Moehrendorf, Germany) (E), the design of which is shown in Figure 6.2 [41][42]. The thorax phantom simulates normal tissue, lungs and bone in the thoracic area, including the spine. In the center, it has a cylindrical hole, in which a static phantom, dedicated for scoring calibration, fits in as well. This is the part in which the water tank is implemented, and in which the lesion phantom is moving. The thoracic phantom's dimensions are equivalent to these of a normally sized person.

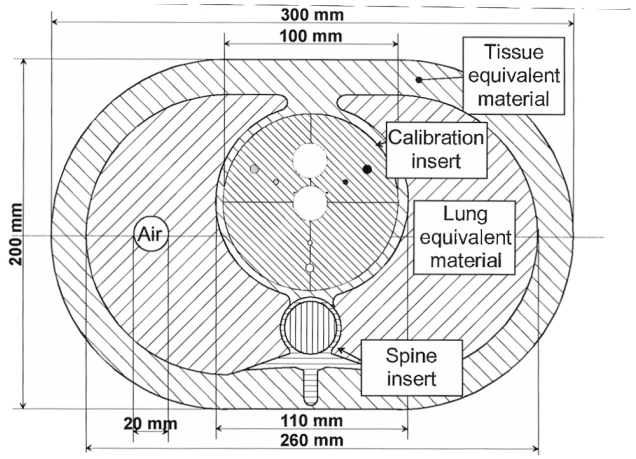

Figure 6.2: *The anthropomorphic thorax phantom with its standard calibration insert.*

The simulator is equipped with a pulse generator (G), which is able to produce ECG equivalent pulses. This allows the system to operate together with the ECG gating module of the CT, since it is compatible with it's conventional ECG monitor. The motion profiles generated, can be synchronized with this R-R pulse accordingly.

The mechanical motion is generated in the black box (A). Each direction (x,y,z) is controlled by a different motor. All together the three motors produce a motion, the characteristics of which can be set and programmed onto the software of the simulator, since it is connected to and managed by a PC device. Each motion profile consists out of four columns, representing time, x, y and z, and can have a maximum of 30 preprogrammed positions. The start and end position of the motion profile have to include the same coordinates.

The motion profiles used in this study, are comparable to normal cardiac movement. The profiles are of equivalent R-R motion at all heart rates, with appropriate time shrinking for 40, 50, 60, 70, 80, 90 and 100 bpm. A position

in all directions and a velocity diagram of a 60 bpm heart rate are showed in Figure 6.3.

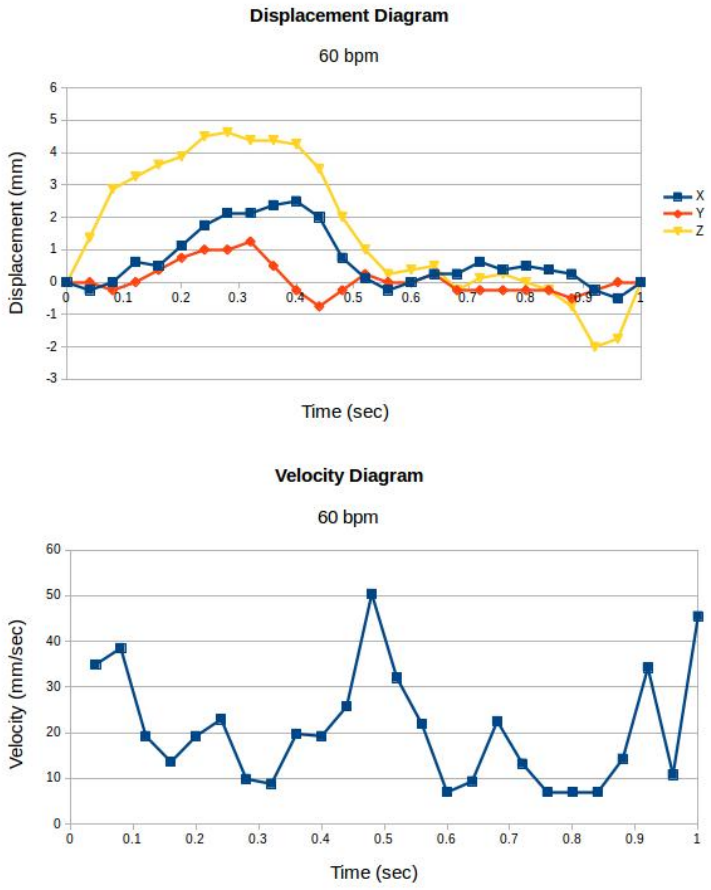

Figure 6.3: *Diagrams of X, Y, Z displacement and Velocity for a 60 bpm simulation.*

As a whole the dynamic phantom has good positioning accuracy, with 0.2 mm static mode accuracy and 0.3% reproducibility error in its dynamic mode. It allows a maximum linear displacement of 90 mm in the x and z axes, and 60 mm displacement in the y axis. Its maximum motion profile frequency is equivalent to 180 bpm.

6.4 Construction of Calcium Phantoms

The construction of calcium phantoms was divided into three stages. First, large scale phantom materials were constructed and measured. Then a phantom

material was selected in order to proceed to the construction of different calcium concentrations which were to give different attenuation intensities. Thereafter, small lesion equivalents were constructed in different sizes. In the end some of the final lesion equivalents were selected and positioned on a construction that could be mounted onto the motion simulator.

Figure 6.4: *Measurement setups of different materials in different stages of the calcium phantom construction.* ***top left:*** *Various different materials taped on a Plexiglas phantom.* ***top right:*** *The first set of small lesion equivalents in small sizes glued onto small plastic sticks.* ***bottom:*** *The final lesion equivalent measurements before the end selection.*

6.4.1 First and Second Stage

The calcium phantoms that had to be created required a material with similar attenuation properties with calcified lesions when imaged in a CT. The first step was to search into materials with either calcium as an ingredient, or ingredients with a similar atomic number. This led to a selection of acrylic and wax mixtures as well as pottery and building materials.

The phantom material to be selected had to possess other qualities as well. Its final state should have to be water proof, since it would have to be imaged into a water tank. Furthermore, it had to be able to adapt to millimeter scale without breaking or losing its physical form, as well as to be sculpturable in that scale in order to form the desired shape. Finally, the perfect material

should be able to appear in different mixture analogies, in order to simulate different calcium densities.

The materials were constructed in centimeter scale sizes and measured in the CT at 120, 100 and 80kV. In order to lower artifacts due to the relatively high attenuation coefficients of the materials, they were taped onto a cylindrical Plexiglas phantom (see Figure 6.4 top left, Figure 6.5 top). The images were then taken and each material was checked for it's maximum, minimum and mean HU output at all voltages. Ideally, the HU minimum had to be over 130 HU in order to be detected as a calcification by the scoring algorithm, the mean had to be between 130 and 500 HU and the maximum should not be much higher than the mean HU and definitely not exceed 1000 HU. These standards were set in order to be close to the AS weight factor scale.

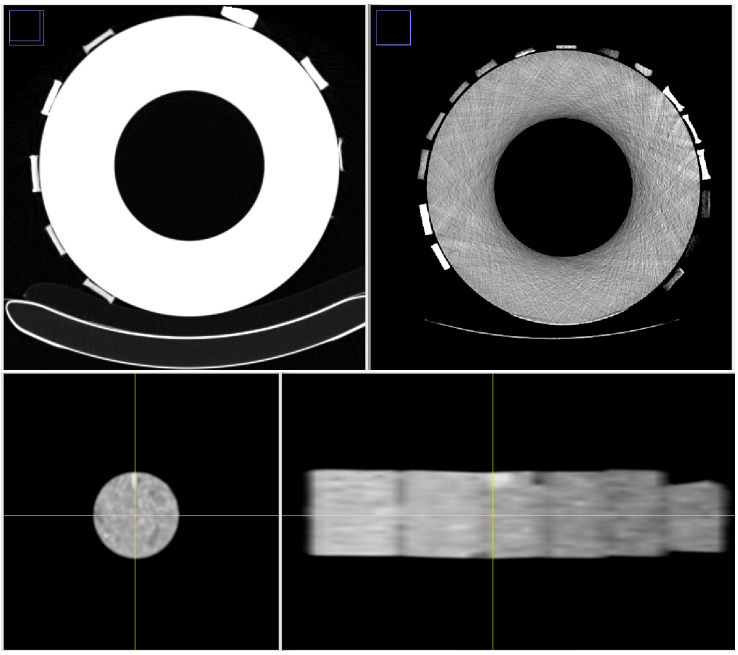

Figure 6.5: *Acquisitions of phantom materials.* ***top****: Various large scale phantom materials taped onto a Plexiglas phantom.* ***bottom****: Paraffin-Calcium Carbonate phantom materials of different analogies in axial and transverse view. The transverse view shows how intensity falls together with the fall in calcium carbonate concentration.*

The material showing most promise was a wax and calcium mixture. It was constructed by simply adding calcium carbonate to molten wax and letting it solidify while returning to room temperature. The material was water proof and easily adaptable to lower scale shapes. Furthermore, the nature of the mixture allowed different wax-calcium analogies, which made the calcium density adaptable according to the needs of the experiment. The construction of

this material however showed a problem in achieving homogeneity. (It is worth mentioning that this defect was not detected until the imaging of the material.) The calcium of the mixture tended to concentrate at the bottom of the material and thus required an alternative mixing methodology.

The solution to the inhomogeneity was inspired by an article by P. Shikhaliev onto spectral CT phantom materials [43]. The mixture was now produced by mixing paraffin with calcium carbonate($CaCO_3$). Paraffin was found in the form of tea candles, while calcium carbonate was in the form of calcium supplement tablets. The process followed was as follows. First a known quantity of $CaCO_3$ was carefully smashed into as thin powder as possible. Thereafter paraffin was brought to approximately $50-60^oC$ and melted (the melting point of paraffin is approx. 37^oC). Once in liquid form, the powder was slowly added to the melted paraffin and stirred for approximately 2-3 minutes. The solid $CaCO_3$ powder does not dilute into the paraffin, however. Therefore, the mixture was poured onto a large metal (non porous) surface and was allowed to solidify again. The mixture was then pulled off the metal surface and smashed into powder again. The next step was to bring the now homogeneous powder into a solid form. Therefore, the powder was tossed into a cylindrical metal form and an approximately 50 kg of pressure was applied upon the powder through a pressure applying device. In that way, the powder was turned into a solid mass.

The final material had all the properties required for the next stage and thereby was easily measured as for its calcium concentration. Since the concentration of the $CaCO_3$ into the material was known, a $mgCaCO_3/cm^3$ concentration was easily calculated simply by measuring the volume of the cylindrical final material. In that way several different $CaCO_3$ concentrations were created and measured (see Figure 6.5 bottom). From this sample, various concentrations were selected and moved to the third stage, the small lesion construction. The measurements of minimum, maximum and mean HU are portrayed in table 6.1.

Statistical analysis of the measured data showed very significant (p-value < 0.001) correlation between the calcium density and the mean HU value and showed a highly significant linear relation between the two values (see Figure

sample	$mgCaCO_3/cm^3$	*mean*	*minimum*	*maximum*
1	420	867.12	603.29	1110.14
2	340	776.02	594.29	971.86
3	240	618.39	275.80	978.40
4	200	480.44	274.60	713.60
5	160	341.42	120.17	653.17
6	100	378.42	175.60	661.40

Table 6.1: The mean, minimum and maximum HU averaged over all the slices on the CT image for each different $CaCO_3$ concentration of the paraffin-calcium carbonate material. The values correspond to a 120 kV acquisition.

6.6).

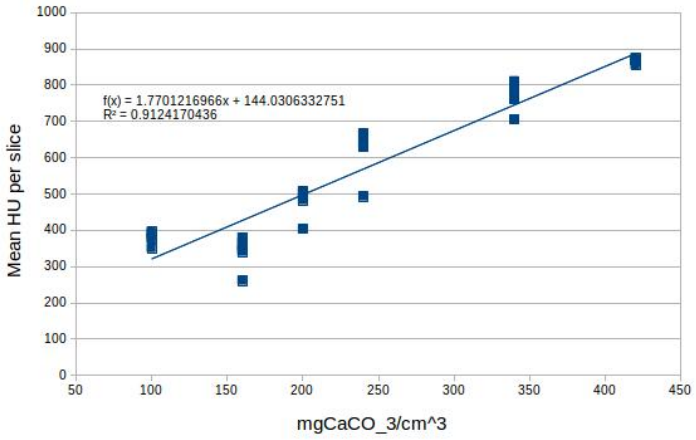

Figure 6.6: *Relation between Mean HU per slice and Calcium Carbonate concentration*

6.4.2 Third Stage

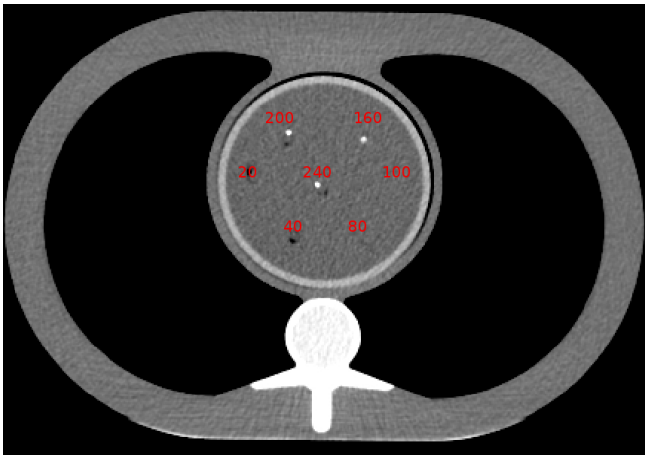

Figure 6.7: *CT imaging of calcium lesion phantoms inside the thorax phantom. The slice was taken from a 120kV acquisition. The numbers represent the concentration of each calcium lesion in* $mgCaCO_3/cm^3$*. It is obvious that the 3 mm lesions are not all visible.*

Calcified lesions appear in all sorts of sizes and shapes. In our case, however, it was decided to proceed with cylindrical shapes. Since lesions appear

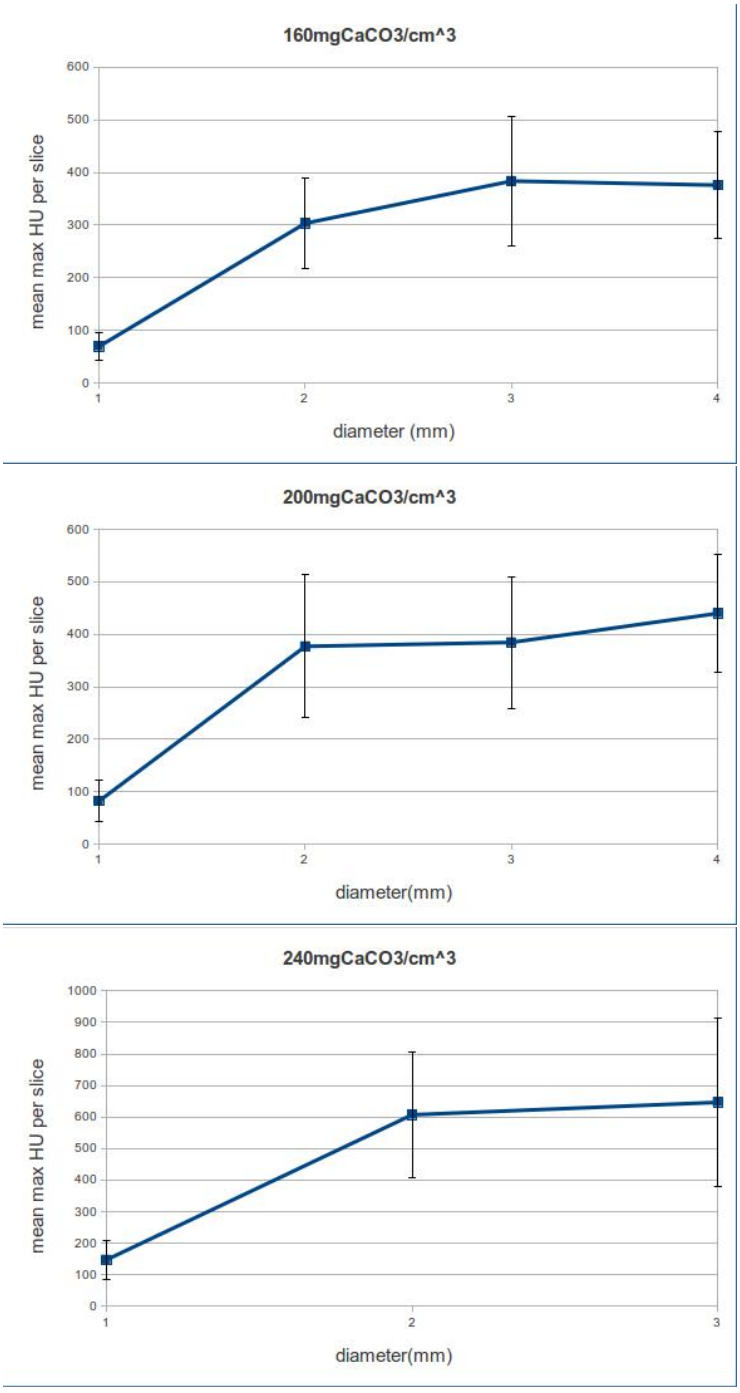

Figure 6.8: *Graphs showing the maximum HU per slice average change as cylinder diameter changes. The cylinders were placed with their long axis parallel to the z-axis of the CT. The graphs correspond to three different calcium carbonate concentrations*

across the coronary arteries and it is known (see Table 3.1) that coronary arteries have a diameter of 2.5 to 5 mm, the lesion equivalents should be of similar diameters. Therefore we constructed lesion phantoms of 1, 2, 3 and 4 mm (see Figure 6.4 top right and bottom). The construction of accurate shapes in this scale proved difficult and was therefore done with the help of a form. The form was made from smooth plastic into which 1, 2, 3 and 4 mm holes were drilled. The calcium equivalent material was again brought into it's powder state and with an analogous method to the large scale construction the small calcium phantoms were made.

Earlier measurements led to the decision to employ $CaCO_3$ concentrations of a 240 $mgCaCO_3/cm^3$ maximum for the calcified lesion phantom construction. The CT scans however showed incapability of the CT system in detecting same HU values as lesion diameter shrunk. This can be seen in Figure 6.8 and in the appendix (.1). Although lesion diameters until 2 mm showed a small and stable drop in HU intensities as diameter lowered, the intensity of 1 mm lesions dropped exponentially. This led only the $240mgCaCO_3/cm^3$ material to be the only one exceeding the 130HU threshold (see appendix .1).

Lower than 160 $mgCaCO_3/cm^3$ concentrations showed HU levels that did not differ from the water background and were thus not visible (see Figure 6.7). Therefore these materials were excluded as well from the final selection.

Since there were only three calcium densities left, we decided to produce multiple cylindrical samples in these three concentrations of 1, 2, 3 and 4 mm diameters. These were imaged and checked for their homogeneity. The most homogeneous phantoms were chosen for the final selection.

6.4.3 Final Selection

The lesion phantom to be created had to be of similar geometry with the other phantom objects provided by the Sim4DCardio constructor. These phantoms were slim sticks with a diameter of 4 mm and had a total length of 75 mm and an effective length of 55 mm. This meant that there was approximately 55 mm available on which to position the lesion phantoms. For practical reasons, it was decided to proceed with uniformly 8 mm length phantoms of varied diameter. This allowed for 5 lesions to be put in parallel onto the custom made stick, with appropriate spacing ($\sim$ 3 mm).

In order to study the CAC scoring behavior at different diameters, three different diameters were selected from same density material. The calcium density chosen was $160mgCaCO_3/cm^3$, since it showed HU maximums into the range of the AS density factor and the available diameters of 2 mm, 3 mm and 4 mm were positioned onto the stick. In order to study the CAC scoring behavior at different calcium densities, a phantom consisting out of a different material density needed to be added to the selection. We therefore chose to add a $200mgCaCO_3/cm^3$ of 2 mm diameter to the stick. We decided to also add the 1 mm $240mgCaCO_3/cm^3$ density material to the selection in order to study the CAC scoring behavior for very thin lesions. The final form of the phantom is portrayed in Figure 6.9.

Figure 6.9: *The final set of calcium lesion phantoms. From left to right: 240mg$CaCO_3/cm^3$ 1 mm, 200mg$CaCO_3/cm^3$ 2 mm, 160mg$CaCO_3/cm^3$ 4 mm, 160mg$CaCO_3/cm^3$ 3 mm, 160mg$CaCO_3/cm^3$ 2 mm. All calcium lesion phantoms have a length of 8 mm.*

The stick onto which the phantom materials were positioned is a plastic straw, which is thin enouqh not to be visible onto the CT imaging device. The phantom materials were glued to the straw with a thin layer of glue which proved invisible as well. The design was made in such a way as to minimize the concentration of bubbles when the stick entered the water tank. The one end of the straw was positioned onto a screw that was adaptable onto the moving arm of the simulator.

6.5 Experimental Setup

The water tank was inserted into the thorax phantom, the mechanical part of the Sim4Dcardio was attached to the water tank and the custom made lesion phantom was screwed onto the moving arm into the water tank. The latter process was carefully done so as to eliminate the presence of air bubbles onto the phantom. The ECG pulse generator was connected to the ECG monitor of the CT and the whole setup was placed onto the patient table, with the phantom spine parallel to the z axis of the CT.

The simulator was operated by a computer in the control room of the CT. The preset motion profiles of 40, 50, 60, 70, 80, 90 and 100 bpm were used and the phantom was scanned according to the CAC scoring protocol for each heart rate simulation.

These 6 acquisitions were loaded into the CAC scoring software and the five separate lesions were tagged separately. This allowed simultaneous CAC scoring of all lesions together, but each lesion separately as well. At the end, the AS, the CMS and the CVS scores of the total calcification as well as all calcifications separately were recorded for each heart rate simulation.

Chapter 7

Results

7.1 Total results

The measured AS, CMS and CVS values for all the lesions are presented in table 7.1. Considering the values taken at 40 bpm as the most accurate, due to having the least motion present, a second table was created. The second table presents the CAC scoring data acquired at each heart rate, divided by the CAC scoring value at a 40 bpm rate, forming a fraction of each measurement relative to the 40 bpm CAC score.

Heart Rate *bpm*	*Total* *AS*	*Total* *CMS*	*Total* *CVS*
40	312	66	165
50	309	65	139
60	295	61	137
70	296	60	139
80	276	56	143
90	296	56	152
100	274	52	125
bpm	$\frac{AS}{AS_{40}}$	$\frac{CMS}{CMS_{40}}$	$\frac{CVS}{CVS_{40}}$
40	1.00	1.00	1.00
50	0.99	0.98	0.84
60	0.95	0.92	0.83
70	0.95	0.91	0.84
80	0.88	0.85	0.87
90	0.95	0.85	0.92
100	0.88	0.79	0.76

Table 7.1: The scores of the total calcium phantom for every heart rate.

Beginning with the AS, we can see a stable score fall as heart rate in-

creases. Starting at a total AS of 312 for 40 bpm, we end up at a 12% lower score of 274 at 100 bpm. This fall seems to be statistically significant (p-value $<$ 0.05), since a linear regression test showed a p-value of 0.018 and an R^2 of 0.704, meaning that the linear model proved significant, while explaining 70.4% of the variation. The model showed a 0.2($\pm$0.1)% score fall ($b_1 = 0.002$ $sd_{b_1} = 0.001$) per unit bpm change. In other words we have statistically significant evidence that for every 10 bpm higher heart rate, a 2% lower AS is expected. In figure 7.1 we can see the graphs describing these results.

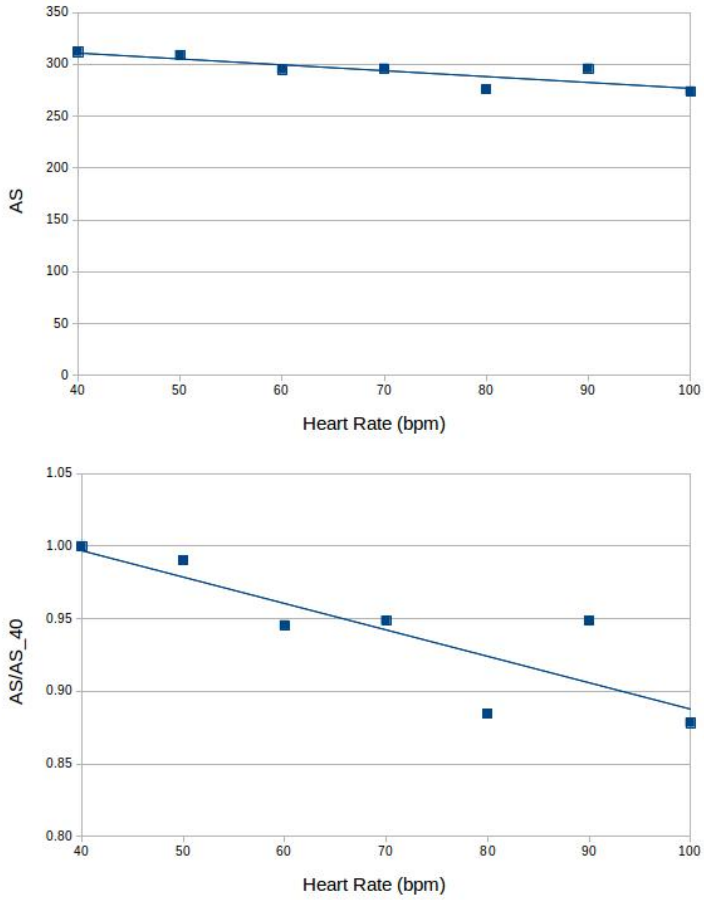

Figure 7.1: *The total AS-HR and total AS/AS_{40}-HR* diagrams. Dots show measured data, while the blue lines show the linear model that describes the drop in AS while HR increases.

For the Calcium Mass Score, we also see a drop in total score. Starting at a 66 CMS for 40 bpm, we end up at a lower 52 CMS for 100 bpm. This re presents a total of 21% fall in score. The statistical evidence here, is even more

important. The linear regression model is of highly significant value, since it's p-value is less than 0.001. Also, an R^2 value of 0.969 shows that the model explains almost all data variations. The linear model shows a fall of $0.4(\pm 0.0)\%$ per unit bpm, or a 4% drop per 10 bpm heart rate increase. In figure 7.2 we can see the graphs describing these results.

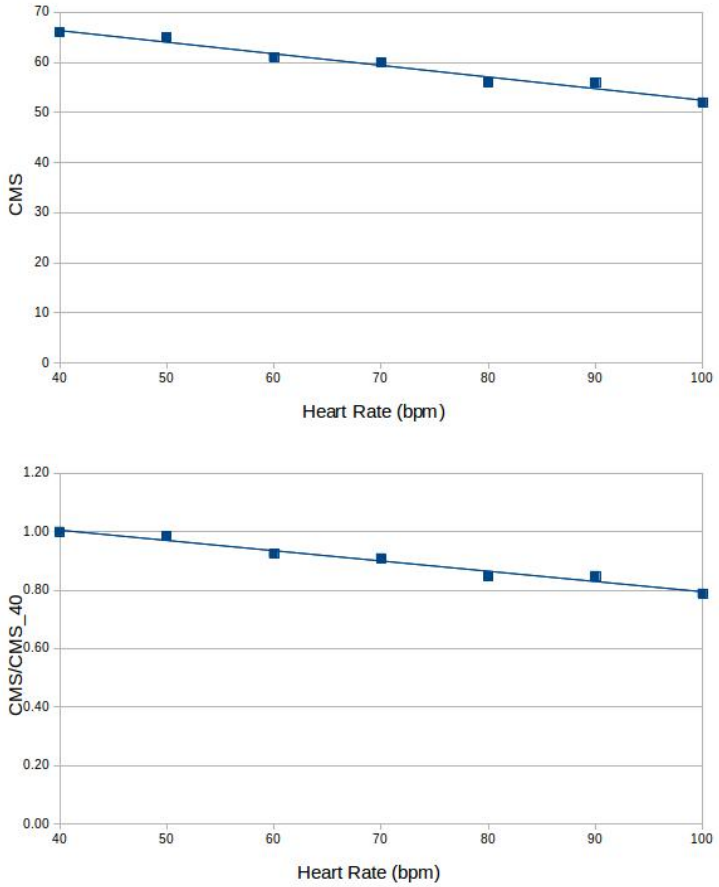

Figure 7.2: *The total CMS-HR and total CMS/CMS_{40}-HR diagrams. Dots show measured data, while the blue lines show the linear model that describes the drop in CMS while HR increases.*

The CVS results are quite different than these of the previous two scores (see Figure 7.3). Although the highest CVS is taken at 40 bpm (165 CVS) and the lowest at 100 bpm (125 CVS) showing signs for a scoring drop as heart rate increases, the rest of the scores in between seem confusing. We observe a significant 16% drop between 40 and 50 bpm, with an almost stable region at 50 to 80 bpm. A linear model does not explain the scores (p-value = 0.213)

and probably more data is required in order to make statements about the CVS behavior.

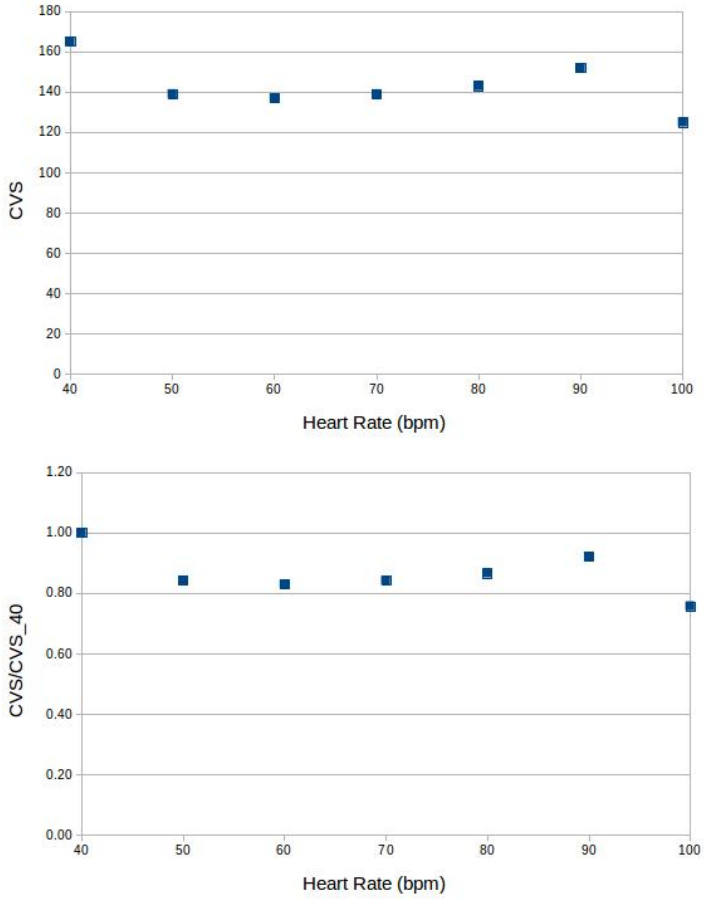

Figure 7.3: *The total CVS-HR and total CVS/CVS_{40}-HR diagrams showing the measured data.*

7.2 Individual lesion results

The individual lesion phantom results are shown in Table 7.2 Here we can see the AS, CMS and CVS taken at each acquisition, for all the different heart rates. This table lets us see in more detail how the scoring systems respond to heart rate change. Our lesion selection allowed for both very low and very high scores and at some points allowed for systematic description of scoring response according to lesion diameter and calcium density. As with the total

scores, fractions of the scores according to 40 bpm scores were included in the table, for better understanding of the franctional change.

$Heart\ Rate$	240 $mgCaCO_3/cm^3$ $1mm$			200 $mgCaCO_3/cm^3$ $2mm$			160 $mgCaCO_3/cm^3$ $4mm$			160 $mgCaCO_3/cm^3$ $3mm$			160 $mgCaCO_3/cm^3$ $2mm$		
bpm	AS	CMS	CVS	AS	CMS	CVS	AS	CMS	CVS	AS	CMS	CVS	AS	CMS	CVS
40	3	2	8	41	8	17	160	33	82	78	16	36	30	7	22
50	5	2	4	33	7	9	156	32	79	83	18	35	32	6	12
60	2	0	2	39	8	13	141	31	78	85	16	33	28	6	11
70	2	1	5	32	6	11	151	31	79	80	16	31	31	6	13
80	3	0	3	37	7	16	144	31	80	75	14	28	17	4	9
90	0	0	0	37	6	14	150	30	81	88	15	32	21	5	25
100	0	0	0	41	6	13	147	29	78	70	13	25	16	4	9
bpm	$\frac{AS}{AS_{40}}$	$\frac{CMS}{CMS_{40}}$	$\frac{CVS}{CVS_{40}}$	$\frac{AS}{AS_{40}}$	$\frac{CMS}{CMS_{40}}$	$\frac{CVS}{CVS_{40}}$	$\frac{AS}{AS_{40}}$	$\frac{CMS}{CMS_{40}}$	$\frac{CVS}{CVS_{40}}$	$\frac{AS}{AS_{40}}$	$\frac{CMS}{CMS_{40}}$	$\frac{CVS}{CVS_{40}}$	$\frac{AS}{AS_{40}}$	$\frac{CMS}{CMS_{40}}$	$\frac{CVS}{CVS_{40}}$
40	1	1	1	1	1	1	1	1	1	1	1	1	1	1	1
50	1.67	1.00	0.50	0.80	0.88	0.53	0.98	0.97	0.96	1.06	1.13	0.97	1.07	0.86	0.55
60	0.67	0.00	0.25	0.95	1.00	0.76	0.88	0.94	0.95	1.09	1.00	0.92	0.93	0.86	0.50
70	0.67	0.50	0.63	0.78	0.75	0.65	0.94	0.94	0.96	1.03	1.00	0.86	1.03	0.86	0.59
80	1.00	0.00	0.38	0.90	0.88	0.94	0.90	0.94	0.98	0.96	0.88	0.78	0.57	0.57	0.73
90	0.00	0.00	0.00	0.90	0.75	0.82	0.94	0.91	0.99	1.13	0.94	0.89	0.70	0.71	1.14
100	0.00	0.00	0.00	1.00	0.75	0.76	0.92	0.88	0.95	0.90	0.81	0.69	0.53	0.57	0.41

Table 7.2: The scores of each individual calcium lesion phantom for every heart rate.

The small 1 mm lesion shows some significant qualitative properties. As can be seen in table 7.2, its very small diameter leads to small scores at 40 to 70 bpm and then stops being detected. This is evidence that indeed the heart rate affects calcium scoring. The linear regression model proves to be significant for all three scores (p-value<0.05) but its low R^2 values are not good enough to approve the models.

In the other lesions the results do not show any statistically significant results about the AS and CVS, although a general qualitative observation can lead us to the same conclusion as with the total scores. The scores seem to be falling for higher heart rates, although more evidence is required in order to prove this hypothesis.

The situation is different, however, in the statistical analysis of CMS. The linear model proves significant for all separate lesions as can be seen in table 7.3.

Calcium Density mg/cm^3	*Diameter*	R^2	b_0	b_1	sd_{b_1}	$P-value$
200	$2mm$	0.596	1.138	−0.004	0.001	0.042
160	$4mm$	0.914	1.061	−0.002	0.000	0.001
160	$3mm$	0.657	1.23	−0.004	0.001	0.027
160	$2mm$	0.782	1.24	−0.007	0.002	0.008

Table 7.3: Results of the linear regression test on the CMS for the separate lesions. b_0 represents the constant of the linear model, b_1 represents the slope of the model and sd_{b_1} is the standard deviation of the slope.

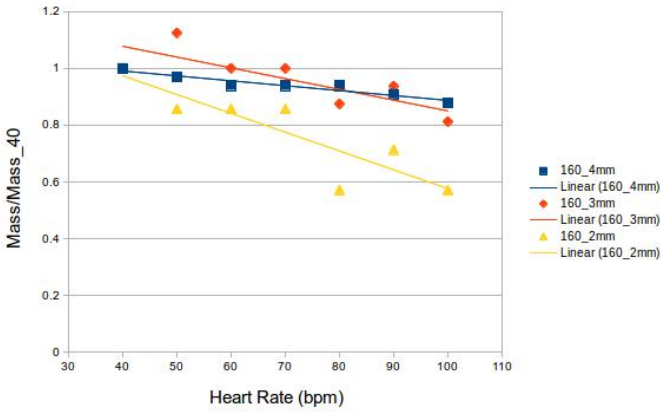

Figure 7.4: *Graph showing the different incline of materials with different diameter*

Accepting the linear regression model for these cases can lead us to two important conclusions. The first conclusion is that as the lesion diameter shrinks, the drop in CMS due to heart rate increase becomes more significant. For a 2 mm lesion with a $160 mgCaCO_3/cm^3$ concentration, the score drops $0.7(\pm 0.2)\%$ per bpm increase, while for 3 mm and 4 mm it drops $0.4(\pm 0.1)\%$ and $0.2(\pm 0.0)\%$ per bpm respectively. This is also portrayed in figure 7.4. The second conclusion is that as the calcium density increases, CMS drop becomes less significant. While for a 2 mm diameter $160 mgCaCO_3/cm^3$ lesion CMS lowers $0.7(\pm 0.2)\%$ per bpm increase, for a same diameter $200 mgCaCO_3/cm^3$ lesion CMS lowers only $0.4(\pm 0.1)\%$ per bpm increase. This is portrayed in figure 7.5.

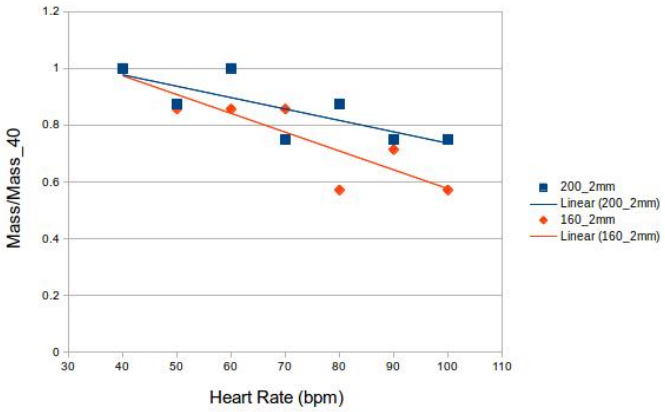

Figure 7.5: *Graph showing the different incline of materials with different calcium concentration*

7.3 Calcium Density Score Results

CDS values based on the 4.3 equation were calculated and are presented in table 7.4. As can be seen both on the table as well as in the graphical representation of the values in Figure 7.6, the CDS values proved very inconsistent as heart rate changed. The values were statistically tested for linearity with no significant result.

The CDS did not present same scoring results for different materials of same calcium density, even when the results were acquired while at the same heart rate. Less variation in CDS values was observed when lesions of larger diameters were measured (see table 3 in the appendices).

Heart Rate *bpm*	$240mg/cm^3$ $1mm$	$200mg/cm^3$ $2mm$	$160mg/cm^3$ $4mm$	$160mg/cm^3$ $3mm$	$160mg/cm^3$ $2mm$	*Total*
40	0.94	6.03	4.88	5.42	3.41	4.73
50	3.13	9.17	4.94	5.93	6.67	5.56
60	2.50	7.50	4.52	6.44	6.36	5.38
70	1.00	7.27	4.78	6.45	5.96	5.32
80	2.50	5.78	4.50	6.70	2.66	4.83
90	–	6.61	4.63	6.88	2.10	4.87
100	–	7.88	4.71	7.00	4.44	5.48

Table 7.4: CDS results for different lesions at different heart rates. The total CDS result represents all lesions combined.

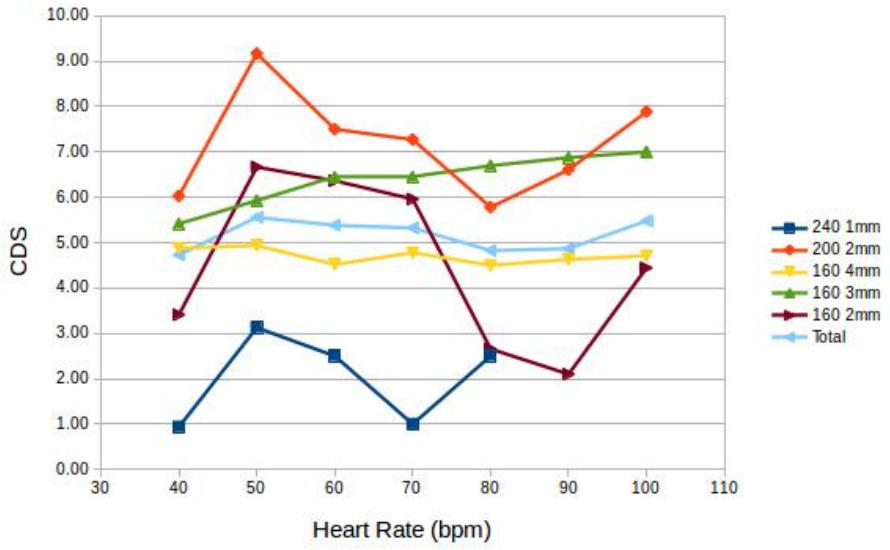

Figure 7.6: *CDS versus heart rate graph including the results of table 7.4*

Chapter 8

Discussion and Conclusion

Earlier work on similar subjects has been done by other research groups. In 2000, Brown et al.[44] reported decreasing AS results with increasing movement on a 4-Slice MDCT.

In 2003, Ulzheimer et al. found that Prospective triggering with 4-slice MSCT scanners is most severely affected by motion, followed by retrospective triggering with 4-slice MSCT, while EBT is least severely affected by motion.[45]

In 2007 and 2008, Groen et al. found CAC-scoring to be strongly influenced by cardiac motion, calcification density, and slice thickness. More specifically, they found CAC scores to be increasing for high density calcifications and decreasing for low density calcifications at increasing heart rates, when scanned on a 64-slice MDCT, a DSCT and a EBCT.[46] [47] They also concluded that EBT is the least susceptible to cardiac motion, followed by DSCT and 64-slice MDCT [47].

In 2009, Greuter et al. found calcium score to be highly dependent on the average density of individual calcifications. They concluded that this dependence is linear. Therefore, a quantitative method could be derived which corrects the measured calcium score for the influence of motion, calcification density, and temporal resolution. They also showed that calcium score on DSCT and 64-slice MDCT is more susceptible to motion as compared to EBT and that CMS is less susceptible to motion compared to CVS and AS.[48]

In 2012, Tigges et al. performed simulations on a 64-slice CT. They found that coronary artery motion significantly affects AS, CVS and CMS, that the effects of motion on each quantification method are similar, that more motion and higher heart rates result in generally lower calcium estimates and that the effect of motion on calcium quantification depends on both the trajectory and magnitude of the motion as well as the heart rate.[49]

From the mentioned articles, only Ulzheimer et al. and Tigges et al. used three dimensional simulation in their study[49]. Tigges et al. had another advantage, namely the use of explanted coronary arteries in their simulation[49]. The rest used a setup similar to the one used in this work, but with one dimensional cardiac motion simulation[46] [47] [48].

Our study found that heart rate affects all three common scoring methods, when applied on 64-slice MDCT 2.5 mm sliced prospectively gated acquisitions. The AS and CMS were found to behave linearly on the large scale (large scores). From these two, CMS showed to be more susceptible to motion (-0.4($\pm$0.0)% bpm) than AS (-0.2($\pm$0.1)%). However the CMS linearity proved highly significant and with very small deviance from the linear model, while the AS model proved less significant. These results are generally in accordance with the available literature. However Greuter et al. had concluded that CMS is less prone to motion than AS [48].

Our study found that heart rate increase causes a less significant CMS drop when Calcium concentration is higher. This is also in accordance with the available literature at the concentrations we studied. Groen et al. and Greuter et al. found that velocity increase can cause a scoring increase when calcium concentration is higher than the densities we studied [46] [47] [48]. However the concentrations we studied are comparable with real CAC densities and provide similar results [49]. Groen et al. explained the CAC score variation as a function of the calcification density as a result of motion blurring[47].

Our study also proved significant evidence about heart rate increase causing more significant CMS drop when the lesion diameter gets smaller. This result was not found in the literature and can be considered the most important finding of this study. Although not recorded earlier, this can be explained by image blurring. An object, when moved at a specific velocity, will widen on the slice, proportionally to the time the CT needed to collect the data required for the specific slice and the distance the object has moved during that period. The distance traveled does not change in different diameters, thus the blurring is not directly proportional to the object's area. Therefore larger diameters produce less blurring and consequently a smaller area widening percentage, resulting in smaller score change.

An analysis of the proposed CDS proved to be susceptible to both lesion diameter and heart rate, more than any conventional scoring method. The CDS aims to give a semi-quantitative indicator of calcium density based on the AS and CVS [38] [39], but its inability to detect similar scores for same density materials when diameter changes makes this scoring method problematic. Its dependency on two different scoring systems (AS and CVS) is probably the reason its behavior in heart rate increase is unpredictable. Overall, the score seems to have limited reproducibility.

Concluding, we found that AS, CMS and CVS are dependent on heart rate. AS and CMS proved to respond linearly to heart rate increase, with heart rate increase decreasing score outcome. In more detail, CMS showed to decrease more with heart rate increase, when calcium density is lower and when lesion diameter is smaller. Finally, the CDS seems to have limited reproducibility and inability to relate to real calcium density.

Chapter 9

Limitations and Further Research

In this study a method was developed to construct calcified lesion phantoms with simple materials. This allows for a lot of further work and research in the area of CAC scoring. Furthermore, some limitations of this work can be overcome and some of the data can be researched in more detail.

The results of this study are based upon one acquisition on each of the seven different heart rates from 40 to 100. This specific research could probably have given more statistically significant information if multiple acquisitions were taken on each heart rate. With more data available, the study could have come to safer or maybe more conclusions.

The calcified lesion phantoms were imaged at a zero heart rate, but the scores were removed from the data. The phantom was taken off the moving arm of the cardiac simulator and placed at the bottom of the water tank in order to achieve zero heart rate. The scoring results led us to the conclusion that due to being in contact with the plastic bottom of the tank might have interfered too much. Images could be taken at zero heart rate with the phantoms onto the moving arm, in order to investigate the score outcome when cardiac movement is absent.

The results of this study are based upon the scoring of five different calcified lesion phantoms. The study could be continued and broadened. For example, more calcium densities could be measured in order to get a better view of the score behavior for a broader spectrum of densities. Furthermore, different sizes could be measured in a broader spectrum of densities, since in this study only one specific density is studied in relation to its calcified lesion size.

Since protocols are appearing at different tube voltages[28] [27] [29], the effects of heart rate could be examined at these protocols. This would however require calibration of the scoring software at these tube voltages.

Since this study revealed a statistically significant linear drop of AS and

CMS score with heart rate increase, a correction factor could be developed in order to remove the heart rate factor from the scoring outcome. This would require a more analytical study of the heart movement and the reaction of different calcium densities and lesion sizes.

Heart movement is simulated in 3D providing a good analogy to real heart movement. However, the different parts of the heart, and as a consequence different coronary arteries, develop different kinetic behaviors [50] [51] [52] [53]. More cardiac motion profiles could be developed, simulating different kinetic behaviors in order to get a better image of how CAC scores respond in different parts of the heart.

Appendices

.1 Table Appendices

		160				200			240	
$1mm$	$2mm$	$3mm$	$4mm$	$1mm$	$2mm$	$3mm$	$4mm$	$1mm$	$2mm$	$3mm$
37	174	276	187	75	149	103	313	93	192	307
50	317	670	485	135	390	394	505	168	562	430
73	344	698	615	126	439	559	579	188	601	468
79	397	660	474	95	467	537	538	161	565	638
77	416	456	482	70	624	483	567	99	710	809
97	339	386	496	43	638	425	511	80	713	946
118	350	345	550	33	527	422	459	89	607	921
107	291	398	527	19	463	400	562	77	689	731
86	284	418	492	44	318	474	456	73	856	628
58	277	387	420	106	219	532	392	154	881	770
43	269	390	406	132	216	458	391	252	733	981
49	282	348	395	106	325	417	503	292	612	888
38	275	359	404	82	314	373	469	260	559	432
58	174	395	391	116	299	214	96	222	105	
	241	190	134		276	146	172	121		
	328	160	139		430	202	450	146		
	312	273	287		387	221	512	150		
	288	300	295		401	201	454	157		
	273	331	280		436	219	435	179		
	286	337	290		404	280	460	149		
	316	374	321		368	329	481	143		
	302	365	422		404	296	525	132		
	301	336	418		437	270	555	154		
	305	337	350		463	301	559	200		
	337	349	355		345	320	507	196		
	285	418	329		193	338	431	133		
	246	488	340		140	356	431	106		
	400	446	389		108	389	470	156		
	442	343	415		366	283	492	157		

160	160	160	160	200	200	200	200	240	240	240
$1mm$	$2mm$	$3mm$	$4mm$	$1mm$	$2mm$	$3mm$	$4mm$	$1mm$	$2mm$	$3mm$
	323	425	530		502	522	458	72		
	406	372	475		471	465	478	84		
	464	359	416		445	476	492	65		
	379	358	402		360	489	418	123		
	208	497	354		271	518	521	151		
	126	560	391		245	492	489	164		
	433	330	384		244	482	450	164		
	406	249	355		179	534	432	166		
	378	214	343		277	520	463	149		
	356	160	296		342	473	511	154		
	302	232	318		360	383	514	161		
	266	456	394		372	148	390	145		
	254	514	393		441	101	160	129		
	276	495	481		396	240	187	125		
	295	461	384		393	300	369	111		
	330	398	327		509	343	428	84		
	336	417	309		488	415	491	67		
	322	486	318		251	451	528	103		
	212	546	303		116	429	472	124		
	111	516	294		303	368	411	118		
	105	462	363		356	417	431	163		
	132	467	280		226	535	458	199		
	166	386	208		231	416	515	190		
	198	309	243		346	375	517	190		
	254	181	265		528	375	567	176		
	355	248	484		621	360	558	176		
	428	315	539		720	115	458	135		
	426	435	499		662	106	155	79		
	416	128			495	413	171	127		
	355	157			479	146	172	91		
	302	339			461	435	126	65		
	280	440			393	485	375	60		
	292	506			466	502	469	133		

		160				200			240	
$1mm$	$2mm$	$3mm$	$4mm$	$1mm$	$2mm$	$3mm$	$4mm$	$1mm$	$2mm$	$3mm$
	343	501			492	294		184		
	418	382			442	382		215		
	387	347			407	401		203		
	318	400			228	510		133		
	131	412			534	546		109		
		407				418		109		
		414				427		96		
		461				462		139		
		470				455		299		
		444				530		355		
		244				583		323		
		82				537		231		
		270				316				
		329								
		367								
		379								
		511								
		535								
		407								
		517								
		702								
		478								
		293								
		244								
		146								
69.29	303.58	383.83	376.07	82	376.98	384.51	439.82	147.58	607.29	646.71
25.96	84.94	123.71	101.12	38.83	136.03	125.57	111.33	60.87	197.70	265.69

Table 1: *Maximum HU per slice per phantom material for* $160mgCaCO_3/cm^3$, $200mgCaCO_3/cm^3$ *and* $240mgCaCO_3/cm^3$ *phantom materials of cylindrical shape. The 1 mm, 2 mm, 3 mm and 4 mm correspond to cylinder diameter. The bottom two rows contain the average HU measured per slice and the standard deviation respectively.*

$Calcium\ Density\ (mg/cm^3)$	$Diameter$	$Scoring\ Type$	R^2	b_0	b_1	sd_{b_1}	$P\ value$
240	$1mm$	AS	0.614	2.214	-0.021	0.008	0.037
240	$1mm$	CMS	0.658	1.607	-0.018	0.006	0.027
240	$1mm$	CVS	0.702	1.362	-0.014	0.004	0.019
200	$2mm$	AS	0.017	0.869	0.001	0.002	0.782
200	$2mm$	CMS	0.596	1.138	-0.004	0.001	0.042
200	$2mm$	CVS	0.001	0.767	0	0.003	0.952
160	$4mm$	AS	0.313	1.012	-0.001	0.001	0.192
160	$4mm$	CMS	0.914	1.061	-0.002	0	0.001
160	$4mm$	CVS	0.094	0.989	0	0	0.504
160	$3mm$	AS	0.091	1.101	-0.001	0.002	0.512
160	$3mm$	CMS	0.657	1.23	-0.004	0.001	0.027
160	$3mm$	CVS	0.771	1.179	-0.004	0.001	0.009
160	$2mm$	AS	0.717	1.458	-0.009	0.003	0.016
160	$2mm$	CMS	0.782	1.24	-0.007	0.002	0.008
160	$2mm$	CVS	0.011	0.792	-0.001	0.006	0.825

Table 2: Results of the linear regression test on all scores for all separate lesions. b_0 represents the constant of the linear model, b_1 represents the slope of the model and sd_{b_1} is the standard deviation of the slope.

	bpm	40	50	60	70	80	90	100
$2mm$	CDS	3.41	6.67	6.36	5.96	2.66	2.1	4.44
40	3.41	0	95.60	86.51	74.78	−60.12	−38.42	30.21
50	6.67	−48.88	0	−4.65	−10.64	−60.12	−68.52	−33.43
60	6.36	−46.38	4.87	0	−6.29	−58.18	−66.98	−30.19
70	5.96	−42.79	11.91	6.71	0	−55.37	−64.77	−25.50
80	2.66	28.20	150.75	139.10	124.06	0	−21.05	66.92
90	2.10	62.38	217.62	202.86	183.81	26.67	0	111.43
100	4.44	−23.20	50.23	43.24	34.23	−40.09	−52.70	0
$3mm$	CDS	5.42	5.93	6.44	6.45	6.7	6.88	7
40	5.42	0	9.41	18.82	19.00	12.98	26.94	29.15
50	5.93	−8.60	0	8.60	8.77	12.98	16.02	18.04
60	6.44	−15.84	−7.92	0	0.16	4.04	6.83	8.69
70	6.45	−15.97	−8.06	−0.16	0	3.88	6.67	8.53
80	6.7	−19.10	−11.49	−3.88	−3.73	0	2.69	4.48
90	6.88	−21.22	−13.81	−6.40	−6.25	−2.62	0	1.74
100	7.00	−22.57	−15.29	−8.00	−7.86	−4.29	−1.71	0
$4mm$	CDS	4.88	4.94	4.52	4.78	4.5	4.63	4.71
40	4.88	0	1.23	−7.38	−2.05	−8.91	−5.12	−3.48
50	4.94	−1.21	0	−8.50	−3.24	−8.91	−6.28	−4.66
60	4.52	7.96	9.29	0	5.75	−0.44	2.43	4.20
70	4.78	2.09	3.35	−5.44	0	−5.86	−3.14	−1.46
80	4.5	8.44	9.78	0.44	6.22	0	2.89	4.67
90	4.63	5.40	6.70	−2.38	3.24	−2.81	0	1.73
100	4.71	3.61	4.88	−4.03	1.49	−4.46	−1.70	0

Table 3: An analysis of the percentage difference between CDS scores taken at different heart rates for the three $160 mgCaCO_3/cm^3$ phantoms of different diameter.

Bibliography

[1] Knoll GF. Radiation Detection and Measurement. John Wiley & Sons; 2010.

[2] Johns HE, Cunningham JR. The physics of radiology. American lecture series. Charles C. Thomas; 1983.

[3] Bushberg JT, Seibert JA, Leidholdt EM, Boone JM. The Essential Physics of Medical Imaging. Wolters Kluwer Health; 2011.

[4] M BT. Computed tomography: From photon statistics to modern cone-beam CT. Springer; 2008.

[5] Bushberg JT, Seibert JA, Leidholdt EM, Boone JM. The Essential Physics of Medical Imaging. Lippincott Williams & Wilkins; 2002.

[6] Hubbell JH, Seltzer SM, of Standards NI,) TUS. Tables of X-ray mass attenuation coefficients and mass energy-absorption coefficients 1 keV to 20 MeV for elements Z=1 to 92 and 48 additional substances of dosimetric interest [electronic resource] / J.H. Hubbell and S.M. Seltzer. Web version. ed. U.S. Department of Commerce, Technology Administration, National Institute of Standards and Technology Gaithersburg, MD; 1996.

[7] J T Littleton MLDL. Conventional Tomography. In: A History of the Radiological Sciences. Radiology Centennial, Inc.; 1996. .

[8] van Gijn J, Gijselhart JP. Ziedses des Plantes: uitvinder van planigrafie en subtractie. Ned Tijdschr Geneeskd. 2011;155(A2164).

[9] Webb S. From the Watching of Shadows, The Origins of Radiological Tomography. Adam Hilger; 1990.

[10] Evens RG. Computed Tomography. In: A History of the Radiological Sciences. Radiology Centennial, Inc.; 1996. .

[11] Dance DR, Christofides S, Maidment ADA, McLean ID, Ng KH. Diagnostic Radiology Physics: A Handbook for Teachers and Students. IAEA; 2014.

[12] Hounsfield GN. Computerized transverse axial scanning (tomography): Part 1. Description of system. The British Journal of Radiology. 1973;46(552):1016–1022. PMID: 4757352.

[13] Rutt BK. Three dimensional scanned projection radiography using high speed computed tomographic scanning system. Google Patents; 1987. US Patent 4,672,649.

[14] Flohr TG, McCollough CH, Bruder H, Petersilka M, Gruber K, Süβ C, et al. First performance evaluation of a dual-source CT (DSCT) system. European Radiology. 2006;16(2):256–268.

[15] Johnson TR, Nikolaou K, Wintersperger BJ, Leber AW, von Ziegler F, Rist C, et al. Dual-source CT cardiac imaging: initial experience. European radiology. 2006;16(7):1409–1415.

[16] McCollough CH, Leng S, Yu L, Fletcher JG. Dual- and Multi-Energy CT: Principles, Technical Approaches, and Clinical Applications. Radiology. 2015;276(3):637–653. PMID: 26302388.

[17] Fuchs T, Kachelriess M, Kalender WA. Direct comparison of a xenon and a solid-state CT detector system: measurements under working conditions. IEEE Transactions on Medical Imaging. 2000 Sept;19(9):941–948.

[18] Shah S, Gnanasegaran G, Sundberg-Cohon J, Buscombe JR, Movahed A, Hall M. Integrating Cardiology for Nuclear Medicine Physicians: A Guide to Nuclear Medicine Physicians. 1st ed. Springer-Verlag Berlin Heidelberg; 2009.

[19] Arthur J-Luciano JV Dorothy-Sherman. Human Physiology. The Mechanisms of Body Function. 8th ed. Boston,MA:McGraw-Hil Higher Education; 2000.

[20] Dodge JT, Brown BG, Bolson EL, Dodge HT. Lumen diameter of normal human coronary arteries. Influence of age, sex, anatomic variation, and left ventricular hypertrophy or dilation. Circulation. 1992;86(1):232–246.

[21] Zeng R. Graphics-sequenced interpretation of ECG. 1st ed. Springer Singapore; 2016.

[22] Mackay J, Mensah GA, Mendis S, Greenlund K, Organization WH. The Atlas of Heart Disease and Stroke. Academic Search Complete. World Health Organization; 2004.

[23] Nichols M, Townsend N, Scarborough P, Rayner M. Cardiovascular disease in Europe 2014: epidemiological update. European Heart Journal. 2014;35(42):2950.

[24] Libby P, Theroux P. Pathophysiology of Coronary Artery Disease. Circulation. 2005;111(25):3481–3488.

[25] Wong ND. Epidemiological studies of CHD and the evolution of preventive cardiology. Nature Reviews Cardiology. 2014;11(5):276–289.

[26] Mendis S, Puska P, Norrving B, Organization WH, Federation WH, Organization WS. Global Atlas on Cardiovascular Disease Prevention and Control. Nonserial Publications Series. World Health Organization in collaboration with the World Heart Federation and the World Stroke Organization; 2011.

[27] Matthew J Budoff JSS Matthew J Budoff. Cardiac CT Imaging: Diagnosis of Cardiovascular Disease. 2nd ed. Springer-Verlag London; 2010.

[28] Nakazato R, Dey D, Gutstein A, Meunier LL, Cheng VY, Pimentel R, et al. Coronary artery calcium scoring using a reduced tube voltage and radiation dose protocol with dual-source computed tomography. Journal of Cardiovascular Computed Tomography. 2009;3(6):394 – 400.

[29] Baron KB, Choi AD, Chen MY. Low Radiation Dose Calcium Scoring: Evidence and Techniques. Current Cardiovascular Imaging Reports. 2016;9(4):12.

[30] ACR-NASCI-SPR PRACTICE PARAMETER FOR THE PERFORMANCE AND INTERPRETATION OF CARDIAC COMPUTED TOMOGRAPHY (CT). 2016;.

[31] Agatston AS, Janowitz WR, Hildner FJ, Zusmer NR, Viamonte M, Detrano R. Quantification of coronary artery calcium using ultrafast computed tomography. Journal of the American College of Cardiology. 1990;15(4):827–832.

[32] Detrano R, Guerci AD, Carr JJ, Bild DE, Burke G, Folsom AR, et al. Coronary calcium as a predictor of coronary events in four racial or ethnic groups. New England Journal of Medicine. 2008;358(13):1336–1345.

[33] Rumberger JA, Brundage BH, Rader DJ, Kondos G. Electron beam computed tomographic coronary calcium scanning: a review and guidelines for use in asymptomatic persons. In: Mayo Clinic Proceedings. vol. 74. Elsevier; 1999. p. 243–252.

[34] Nelson JC, Kronmal RA, Carr JJ, McNitt-Gray MF, Wong ND, Loria CM, et al. Measuring Coronary Calcium on CT Images Adjusted for Attenuation Differences 1. Radiology. 2005;235(2):403–414.

[35] Callister TQ, Cooil B, Raya SP, Lippolis NJ, Russo DJ, Raggi P. Coronary artery disease: improved reproducibility of calcium scoring with an electron-beam CT volumetric method. Radiology. 1998;208(3):807–814. PMID: 9722864.

[36] Hong C, Becker CR, Schoepf UJ, Ohnesorge B, Bruening R, Reiser MF. Coronary Artery Calcium: Absolute Quantification in Nonenhanced and Contrast-enhanced Multi–Detector Row CT Studies. Radiology. 2002;223(2):474–480. PMID: 11997555.

[37] Hoffmann U, Siebert U, Bull-Stewart A, Achenbach S, Ferencik M, Moselewski F, et al. Evidence for lower variability of coronary artery calcium mineral mass measurements by multi-detector computed tomography in a community-based cohort—consequences for progression studies. European journal of radiology. 2006;57(3):396–402.

[38] Sandfort V, Bluemke DA. {CT} calcium scoring. History, current status and outlook. Diagnostic and Interventional Imaging. 2017;98(1):3 – 10.

[39] MH C, JO D, JH I, et al. Calcium density of coronary artery plaque and risk of incident cardiovascular events. JAMA. 2014;311(3):271–278.

[40] Langner O, Hoedlmayr W, Ertel D, Kyriakou Y, Kalender W. A Simulator for Organ Motion Studies in Medicine: Simulation of 3D Rhythmic and Arrhythmic Coronary Artery Motion to Assess Image Quality in Cardiac CT. Proceedings of RSNA Annual Meeting 2007;.

[41] McCollough CH, Ulzheimer S, Halliburton SS, Shanneik K, White RD, Kalender WA. Coronary Artery Calcium: A Multi-institutional, Multimanufacturer International Standard for Quantification at Cardiac CT. Radiology. 2007;243(2):527–538. PMID: 17456875.

[42] McCollough CH, Primak AN, Saba O, Bruder H, Stierstorfer K, Raupach R, et al. Dose Performance of a 64-Channel Dual-Source CT Scanner. Radiology. 2007;243(3):775–784. PMID: 17446525.

[43] Shikhaliev PM. Dedicated phantom materials for spectral radiography and CT. Physics in Medicine and Biology. 2012;57(6):1575.

[44] Brown S, Hayball M, Coulden R. Impact of motion artefact on the measurement of coronary calcium score. The British journal of radiology. 2000;73(873):956–962.

[45] Ulzheimer S, Kalender WA. Assessment of calcium scoring performance in cardiac computed tomography. European radiology. 2003;13(3):484–497.

[46] Groen JM, Greuter MJ, Schmidt B, Suess C, Vliegenthart R, Oudkerk M. The influence of heart rate, slice thickness, and calcification density on calcium scores using 64-slice multidetector computed tomography: a systematic phantom study. Investigative radiology. 2007;42(12):848–855.

[47] Groen JM, Greuter MJ, Vliegenthart R, Suess C, Schmidt B, Zijlstra F, et al. Calcium scoring using 64-slice MDCT, dual source CT and EBT: a comparative phantom study. The international journal of cardiovascular imaging. 2008;24(5):547–556.

[48] Greuter M, Groen J, Nicolai L, Dijkstra H, Oudkerk M. A model for quantitative correction of coronary calcium scores on multidetector, dual source, and electron beam computed tomography for influences of linear motion, calcification density, and temporal resolution: A cardiac phantom study. Medical physics. 2009;36(11):5079–5088.

[49] Tigges S, Arepalli CD, Tridandapani S, Oshinski J, Kurz CR, Richer EJ, et al. A phantom study of the effect of heart rate, coronary artery displacement and vessel trajectory on coronary artery calcium score: potential for risk misclassification. Journal of cardiovascular computed tomography. 2012;6(4):260–267.

[50] Lu B, Mao SS, Zhuang N, Bakhsheshi H, Yamamoto H, Takasu J, et al. Coronary artery motion during the cardiac cycle and optimal ECG triggering for coronary artery imaging. Investigative radiology. 2001;36(5):250–256.

[51] Hofman M, Wickline SA, Lorenz CH. Quantification of in-plane motion of the coronary arteries during the cardiac cycle: implications for acquisition window duration for MR flow quantification. Journal of Magnetic Resonance Imaging. 1998;8(3):568–576.

[52] Husmann L, Leschka S, Desbiolles L, Schepis T, Gaemperli O, Seifert B, et al. Coronary Artery Motion and Cardiac Phases: Dependency on Heart Rate—Implications for CT Image Reconstruction 1. Radiology. 2007;245(2):567–576.

[53] Achenbach S, Ropers D, Holle J, Muschiol G, Daniel WG, Moshage W. In-Plane Coronary Arterial Motion Velocity: Measurement with Electron-Beam CT 1. Radiology. 2000;216(2):457–463.